Effect of Mooring Line Layout on the Loads of Ship-shaped Offshore Installations

M.P. Mujeeb-Ahmed [a], José Cabrera [b], Hyeong Jin Kim [c] and Jeom Kee Paik [c,d,e,*]

[a] *Maritime Safety Research Centre (MSRC), Department of Naval Architecture, Ocean and Marine Engineering, University of Strathclyde, Glasgow G4 0LZ, UK*

[b] *Department of Civil and Environmental Engineering, Universidad de las Américas Puebla, San Andrés Cholula 72810, México*

[c] *Department of Naval Architecture and Ocean Engineering, Pusan National University, Busan 46241, Republic of Korea*

[d] *The Korea Ship and Offshore Research Institute (The Lloyd's Register Foundation Research Centre of Excellence), Pusan National University, Busan 46241, Republic of Korea*

[e] *Department of Mechanical Engineering, University College London, London WC1E 7JE, UK*

* Corresponding Author. Tel: +82 51 510 2429, Mobile: +82 10 3853 8757, Fax: +82 51 518 7687

E-mail addresses: mujeeb.mughadar-palliparambil@strath.ac.uk (M.P. Mujeeb-Ahmed), jose.cabrera@udlap.mx (J. Cabrera), khj94@pusan.ac.kr (H.J. Kim), j.paik@ucl.ac.uk (J.K. Paik).

Abstract

An offshore mooring system stations a ship-shaped offshore installation in place while withstanding incoming loads from the marine environment with short-term and long-term uncertainties. This study aims to develop a novel framework for analysing the loads on floating systems, namely mooring line tension, mooring line fatigue damage, and hull bending moment, as a function of the mooring layout design variables and environmental random variables. The nonlinear influence of those variables is assessed by means of advanced techniques using response charts, response divergence charts, and Sobol's total-effect sensitivity indexes. The developed procedure includes a probabilistic selection of mooring scenarios, station-keeping numerical analyses, and metamodel selection to define input loads. An example of a hypothetical floating production storage and offloading (FPSO) unit with taut legs in the Gulf of Mexico illustrates the procedure. The details of the computations are documented, and the findings show that the mooring line top-tension has a high total-effect index for the wave-induced bending moment and the total mooring line tension, whereas the fatigue damage is mostly affected by the chain diameter. The results of this research offer useful insights to designers and proposes the use of a surrogate model to be used in the reliability-based design of mooring systems.

Keywords: offshore mooring system; ultimate limit state (ULS); fatigue limit state (FLS); design and analysis of simulation experiments (DASE); Sobol's sensitivity analysis.

Abbreviations: ANN, artificial neural network; BK, blind Kriging; CoG, centre of gravity; DASE, design and analysis of simulation experiments; DV, design variable; FLS, fatigue limit state; FPSO, floating, production, storage and offloading unit; LHS, Latin hypercube sampling; MCS, Monte Carlo simulation; OWT, offshore wind turbine; PCE, polynomial chaos expansion; PDF, probability density function; PDM, peak distribution method; POT, Peak Over Threshold Method; RMSE, root mean square error; RV, random variable; SPM, single point mooring system; TLP, tension-leg platform; UK, universal Kriging; ULS, ultimate limit state; WEC, wave energy converter.

Nomenclature

B_i	basis function
b_j	activation function
D	divergence
d	fatigue damage rate / number of synapses between hidden layer and output layer
$f(\mathbf{x})$	trend function
g_{NG}	non-Gaussian peak factor
g_H	peak factor for hardening non-Gaussian process
g_S	peak factor for softening non-Gaussian process
H_s	significant wave height
k	number of variables in the design of experiments matrix
M_w	wave-induced bending moment
m	number of mooring lines per cluster
m_T	total number of mooring lines
N_i	number of cycles to failure at the constant stress range
n	number of scenarios in the design of experiments matrix
n_i	number of cycles for i-th stress range
RMSE	root-mean square error
$s_{j;-j}$	total-effect index
T	tension
T_z	zero-crossing wave period
t	time

v_j	linear mapping between input and hidden layer
$v_Y^+(\mu_Y)$	average mean up-crossing rate
w_{ji}	weight connection between neurons in hidden layer and input layer
$w(\mathbf{x}_j)$	response for the *j*-th scenario
$\mathbf{w}_i$	*i*-th response vector
X_i	random variable
$\mathbf{X}$	random vector
$\mathbf{x}$	input variables vector
$\mathbf{x}_i$	scenario or computer experiment vector
X	design of experiments matrix
Y	random load
$Y(t)$	stochastic process
Y_e	short-term extreme response
y	response
$\hat{y}$	metamodel
$\hat{y}_{\mathrm{ANN}}$	artificial neural network model
$\hat{y}_{\mathrm{BK}}$	Blind Kriging metamodel
Y	response matrix
β_i	coefficient
γ_3	skewness
γ_4	kurtosis
$\delta(\mathbf{x})$	zero-mean Gaussian process of Kriging metamodel

ϑ angle between mooring lines of the same cluster

μ_Y mean

ρ correlation function

$\mathbf{\Sigma}$ correlation matrix of old points outputs

$\boldsymbol{\sigma}(\mathbf{x})$ covariance vector between outputs of old points and new point

σ_Y standard deviation

$\sigma_{\dot{Y}}$ standard deviation for the time derivative

τ duration of simulation

$\mathbf{1}$ all-ones vector

1. Introduction

Ship-shaped offshore installations such as *floating production storage and offloading* (FPSO) units operate in deep and ultra-deep water regions to extract oil and gas in the remote locations. The mooring system of such structures has the function of keeping the floater in position, comprising mooring lines and anchors (Montes-Iturrizaga et al., 2012).

At the early design stage of mooring systems, one of the challenges is defining the *design variables* (DVs) such as materials, anchor positions, line diameter, and line length. Like other marine structures, moored floating systems must be able to withstand the harsh environmental loads coming from waves, wind, and current. However, the life-cycle costs must be kept low, considering initial costs, operational costs, and future costs arising from the mooring system failure. Therefore, setting a *mooring layout* by taking into account uncertainty and consequences is essential to reduce costs without jeopardising safety. In this paper, the former is addressed.

Scholars have developed various techniques for assessing the safety of offshore mooring systems. To mention a few early studies, Sengupta and Ahmad (1996) used *Monte Carlo simulation* (MCS) and Newmark's β method in the nonlinear dynamic analysis of a *tension leg platform* (TLP) to assess the structural reliability of the mooring system and also to predict the service life. Later, Mathisen and Larsen (2004) developed an algorithm for optimising mooring inspection planning by introducing random variables into a crack growth model while considering inspection costs. Vazquez-Hernandez et al. (2006) performed a benchmark study of Level I reliability analyses considering extreme sea states with associated return period, worst sea state from contour lines, and analysis based on response statistics; they concluded that the response-based approach, although more computationally expensive, results in accurate calculation of the reliability index.

Recently, one of the most employed approaches is the use of genetic algorithms for solving multi-objective optimisation problems. Concerning spread mooring systems, early studies where a genetic algorithm for optimisation of a mooring system can be attributed to Yu and Tan (2005) and Shafieefar and Rezvani (2007). Later, Yan et al. (2018) employed a genetic algorithm to optimise a spread mooring system with submerged buoys for a semi-submersible platform; accordingly, they found the optimum design parameters, including buoys' sizes and positions. Tang et al. (2019) analysed the positioning mooring system to install a jack-up platform during towing and positioning operations; the system was optimised in order to derive an appropriate tension and length of the lines.

With the advent of offshore renewable energy projects, advanced methodologies have been developed for the analysis and design of mooring systems. Pillai et al. (2019) coupled a random forest model with a genetic algorithm to minimise the cost and fatigue damage of a spread mooring system for a semi-submersible floating offshore wind turbine (OWT). Ringsberg et al. (2020a) defined two optimum mooring layouts for a floating point-absorbing *wave energy converter* (WEC) by proposing 22 conceptual layouts and reducing the number of candidates employing the Pugh and Kesselring matrices procedure. Extensive research can be found on the validation of the numerical analysis for the motions of a taut-moored WEC and the forces on the lines employing full-scale measurements (Ringsberg et al., 2020b) and wave basin experiments (Yang et al., 2020, 2018).

Focusing on *single point mooring* (SPM) systems (in which all mooring lines are attached to a single point at the floater), Ryu et al. (2016) used the gradient-free harmony algorithm to optimise the initial costs associated with the SPM for FPSOs. Similarly, Schut and Dam (2016) employed the harmony algorithm to minimise the load on the turret chain table for an FPSO in deep water and harsh environment. Cabrera-Miranda et al. (2018) developed a probabilistic approach for estimating the loads on disconnectable mooring systems for FPSOs; they defined a disconnection criterion by minimising life-cycle costs. Li et al. (2019) used a Kriging model with a gradient-based algorithm for minimising the material weight of a mooring system; they applied the methodology for determining line section lengths, diameters, and anchor position of an SPM system for a vessel-shaped offshore fish farm.

Despite the growing body of literature on optimisation of mooring layouts, a qualitative approach for assessing how the DVs influence the loads on the floating system is still lacking. Existing studies have focused on robust design methods that systematically find the combination of DVs that result in the best performance of a mooring system, minimising costs and maximising safety. Nevertheless, the effects of the input variables and their interactions on the loads and other output variables have often been left out of the discussion.

This paper presents a novel framework for assessing the influence of the DVs defining a mooring layout on the loads of floating systems. We propose the use of *response charts* and *response divergence charts* to describe the nonlinear behaviour of loads as a function of several input variables. Next, we conduct *Sobol's sensitivity analysis*, to calculate variance-base indexes in order to rank the input variables according to their importance for the loads. Furthermore, we use *metamodels*, namely *artificial neural networks* (ANN) models and *Kriging* models, to accurately predict the loads while alleviating the computational cost. Since the proposed methodology is rare in the analysis of offshore systems, it is expected that this work will generate fresh insight into the aforementioned area of research.

In the applied example, the target structure of this study is a ship-shaped FPSO installed in ultra-deep water. FPSOs are floating offshore installations that store oil in tanks located in their hulls and periodically offload the petroleum to shuttle tankers, and for construction speed, they are based on converted tankers (Ozguc, 2020; Paik and Thayamballi, 2007). Furthermore, in our application of interest: (1) the mooring system consists of the SPM type with taut mooring lines organised in clusters, (2) the loads are a function of DVs that define the mooring layout and (3) uncertainty from the sea environment are taken into account. Said uncertainties are taken into account in the short-term and long-term by means of the Moment-based Translation model (Ding and Xinzhong, 2016; Hao and Yang, 2020) and probabilistic scenario sampling techniques, respectively. Motivated by the results of previous studies (Cabrera-Miranda et al., 2018; Noble Denton Europe Ltd, 2001), we investigate the loads for the *ultimate limit state* (ULS) and *fatigue limit state* (FLS) for the mooring lines, and the ULS for the FPSO's hull.

Even though the present work deals with ship-shaped offshore floating structures, the proposed procedure is general, and thus, it can be applied in probabilistic-based analyses of other offshore and onshore structures.

The remainder of this paper is organised as follows. Section 2 presents the proposed framework and a detailed description of the procedure followed in this investigation. Section 3 introduces an applied example and gives details on the computation of numerical analyses and metamodels to predict the loads. In Section 4, results for numerical analysis are presented in the form of response and response divergence charts, and the sensitivity analysis to rank the importance of the input variables for the loads. Conclusions are finally given in Section 5.

2. Methodology

We propose the procedure presented in Fig. 1 to investigate the influence of the design parameters.

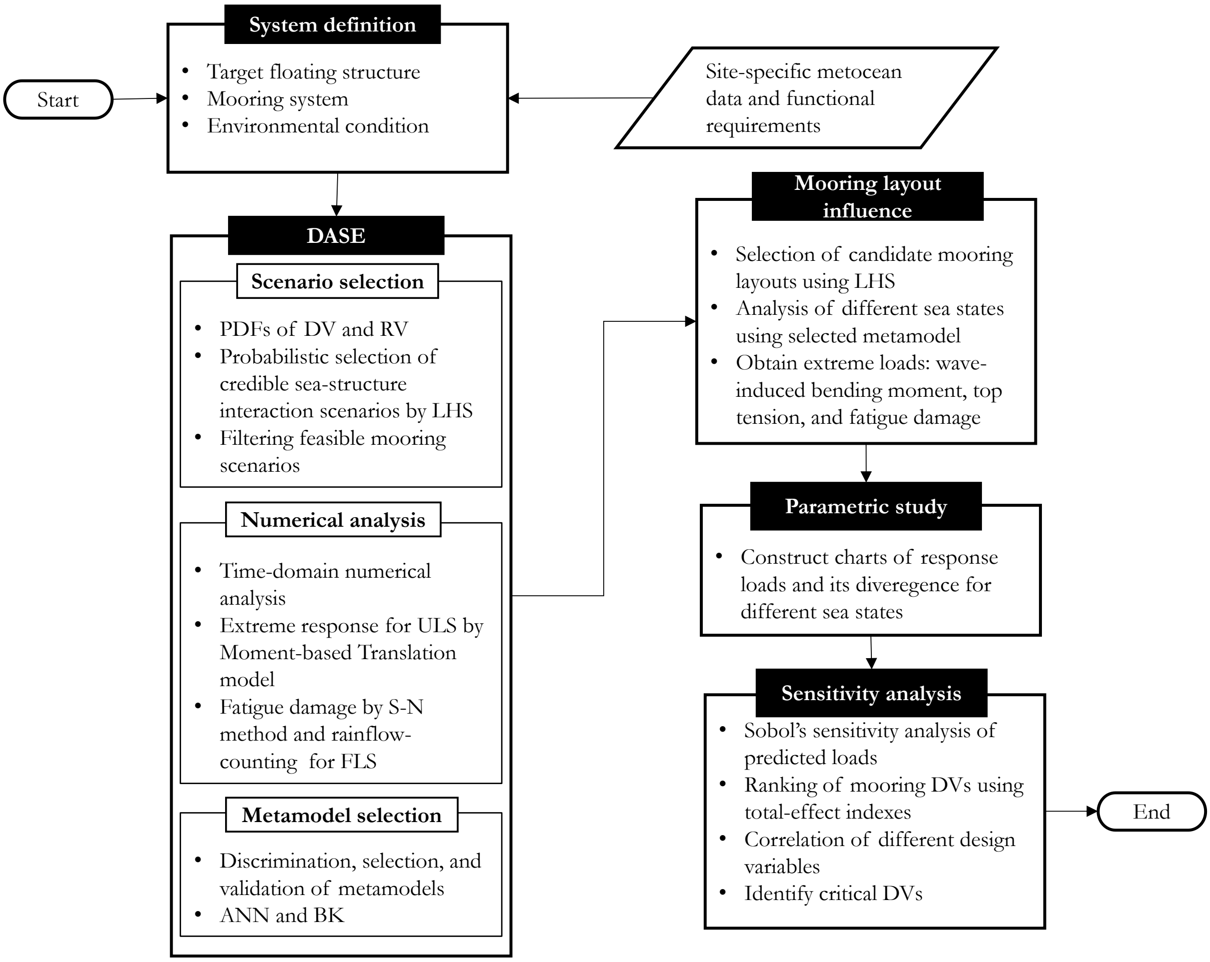

Fig. 1. Proposed novel probabilistic framework for investigating the effect of the mooring layout.

2.1. System definition

A mooring layout of offshore structures is defined here by a set of DVs as illustrated in Fig. 2. In the context of robust design (Fang et al., 2006), the performance of a system can be improved by selecting an appropriate combination of DVs or control factors. For a floating system, DVs can be chosen to reduce the hull loads and mooring line loads, thereby improving reliability.

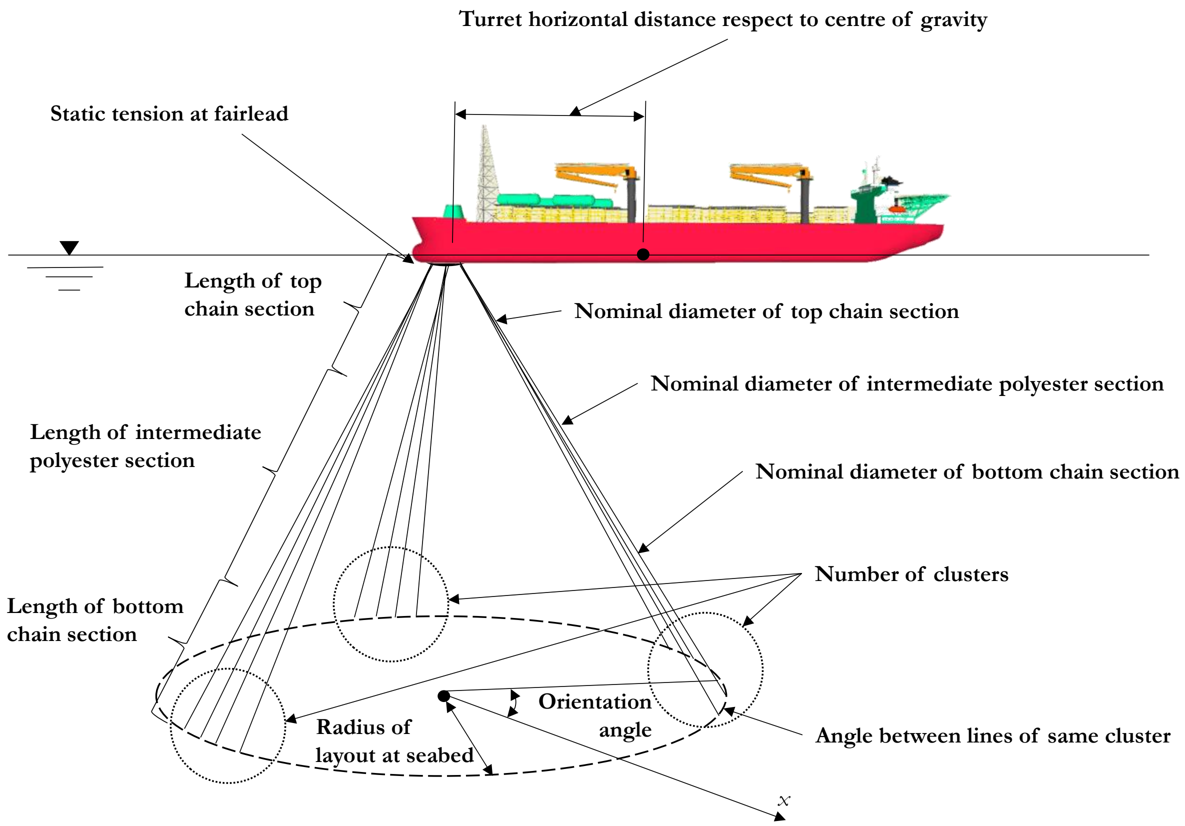

Fig. 2. An illustration depicting various design variables for a taut mooring system of an FPSO. The main direction of environmental loads is aligned with the *x*-axis.

Regarding the probabilistic characterisation of the DVs, uniform distributions are assumed; this is a common approach for variables characterisation in the absence of previous knowledge on their likelihood (Kleijnen, 2017). Besides traditional DVs such as diameter and position of mooring lines, the position of the turret with respect to the *centre of gravity* (CoG) is explicitly investigated. Research on the turret position has shown a significant influence on the hydrodynamic performance of moored ship-shaped floating structures, in particular, heave (Thiagarajan and Finch, 1999) and yaw motions (Sanchez-Mondragon et al., 2018; Xie et al., 2015).

Long-term uncertainties arising from waves, winds, and currents are defined by *random variables* (RVs), which are characterised by a *probability density function* (PDF) based on site-specific metocean conditions. Additionally, the vessel's draft is also included as an RV, since an increment of the draft may result in a raise of the mass and drift force (Liu, 2020; Liu and Papanikolaou, 2020).

2.2. DASE for predicting ULS and FLS loads

2.2.1. Scenario sampling

The *design and analysis of simulation experiments* (DASE) start by selecting several credible scenarios or *computer experiments* to be simulated in the station-keeping analysis. This is done here through the *Latin hypercube sampling* (LHS) technique, in which the general idea is to divide each input into disjoint subsets of equal probability (Shields and Zhang, 2016).

With aforementioned step, a design matrix X of n scenarios and k input variables are computed. Details on the application of LHS in the analysis of offshore installations, in particular, for risk analysis, can be found in the literature (Mujeeb-Ahmed and Paik, 2021, 2019; Paik et al., 2011; Seo et al., 2013).

2.2.2. Mooring system dynamic analysis

Afterwards, the global dynamic analysis of the moored floating structure is conducted for each scenario (row) in $\mathrm{X} = [\mathbf{x}_1, \ldots, \mathbf{x}_n]^{\mathrm{T}}$. The responses, which are loads for our application, are stored in the response matrix Y =[$\mathbf{w}_1,\ldots,\mathbf{w}_s$] for s observed responses in n simulations, where $\mathbf{w}_i$=[$w(\mathbf{x}_1),\ldots,w(\mathbf{x}_n)$]$^{\mathrm{T}}$ are the response vectors.

In the station-keeping analysis, random waves, unsteady wind, and current will result in time-varying forces acting on the floater's hull and mooring lines. Moreover, the associated nonlinearities of the moored floater need to be considered. In this study, the software ANSYS-Aqwa is employed to conduct time-domain simulation under extreme wave conditions whilst considering relevant nonlinearities, such as wave-induced slow-drift force, nonlinear hydrodynamic drag forces on the mooring lines, geometric nonlinear characteristic of the catenary mooring with resulting nonlinear horizontal stiffness of the system, and fully coupled floater-cable dynamics (ANSYS, 2020). A thorough discussion of the adopted approach can be found in a different study (Paik et al., 2015).

For estimating ULS loads, extreme values for wave-induced hull bending moment and mooring line tension is derived from the simulated time histories. Because the responses of a floating mooring system are essentially non-Gaussian, the Moment-based Translation model can be used. The extreme short-term response (Y_e) for a non-Gaussian process $Y(t)$ is given by (Kwon and Kareem, 2011):

$$Y_e = \mu_Y + \sigma_Y\, g_{NG}\left[\nu_Y^+(\mu_Y), \tau, \gamma_3, \gamma_4\right], \tag{1}$$

where t denotes the time, μ_Y is the mean, σ_Y is the standard deviation of the stochastic process estimated from one simulation of duration τ , usually set to 3 hours for offshore calculations. Furthermore, g_{NG} is the non-Gaussian peak factor as a function of the number of the average mean up-crossing rate $\nu_Y^+(\mu_Y) = \sigma_{\dot{Y}} / (2\pi\sigma_Y)$, the skewness of the process (γ_3), and its kurtosis (γ_4), where $\sigma_{\dot{Y}}$ denotes the standard deviation for the derivative of $Y(t)$.

The peak factor in Eq. (1) is a nonlinear transformation of the classical most probable extreme value for a Gaussian process (Naess and Moan, 2013), from the standard normal space to a standard non-Gaussian space. This transformation is achieved by using the moments of the process and Hermite polynomials. Here, we use Winterstein's model (Ding and Xinzhong, 2016; Hao and Yang, 2020) for cases with $\gamma_4 \geq 3$ and the moment-based translation model by Ding and Xinzhong (Ding and Xinzhong, 2016) when $\gamma_4 < 3$, regarded as *softening* and *hardening non-Gaussian processes*, respectively.

While other approaches are available for estimating the short-term extreme response, the advantage of using Moment-based Translation Model is that the full data in the signal of a non-Gaussian process can be employed, and that the estimation of the most probable extreme value is independent of the definition of the peaks, which is an issue in the Peak Distribution Method (PDM) [see for instance Stanisic et al. (2018)]. Another advantage of using the Moment-Based Translation Model is that the estimated short-term extreme response is based on all available observations, and thus, the effect of outliers coming from the transient response due to initial conditions in the simulation is diminished. Recently, the Moment-based Translation model has gained popularity to estimate in Wind Engineering applications (Hao and Yang, 2020; Peng et al., 2020). Other approaches for estimating the short-term extreme of a stochastic process, and in particular for mooring line extreme tension, comprise the Peak Over Threshold Method (POT) (Zhao and Dong, 2020), the already mentioned PDM (Stanisic et al., 2019, 2018), and the global maxima approach based on a Gumbel distribution (DNV GL, 2020) [also discussed by Zhao and Dong (2020)].

Concerning FLS loads, repeated cycles of stress on the mooring lines may cause fatigue damage to accumulate over the years. Applying the S-N method, the stress signal is decomposed into a series of turning points and subsequently analysed using the rain-flow counting algorithm to obtain the number of cycles for various stress ranges n_i (Niesłony, 2009). Then, the fatigue damage rate (d) is calculated by using the Palmgren-Miner's rule as

$$d = \frac{1}{\tau}\sum_{i=1}^{I}\frac{n_i}{N_i}, \tag{2}$$

where N_i is the number of cycles to failure at the constant stress range, τ is the duration of the analysed sea state, and $i = 1,\ldots, I$ is the number of stress ranges considered in the calculation. In this study, the values for N_i are taken from the S-N curves available in the Offshore Standard DNVGL-OS-E301 (DNV GL, 2020).

For fatigue calculations, the long-term variation of the environment needs to be characterised. Usually, the environmental conditions defining a sea state are described by their PDF or are presented in the form of scatter diagrams that provide the frequency of occurrence of the environmental parameters. In this study, we use the PDFs of the significant wave height, the zero-crossing mean period, and other variables associated with wind and current conditions. Then, credible scenarios are sampled by means of LHS, where each scenario captures a sea state suitable for fatigue calculations.

2.2.3. Kriging model and ANN model for predicting loads

Metamodeling is the process of selecting the appropriate surrogate model to predict a linear or nonlinear relationship between several inputs and their output. This process includes choosing candidate models and assessing their accuracy to select a final metamodel on a case-by-case basis. Metamodels are also known as *surrogate models* or *emulators*. The ideal metamodel would perform well both as interpolator and extrapolator in the domain of interest of the input variables, and then, it can be used in parametric studies, reliability-based design, optimisation, and other probabilistic studies.

To name a few applications of metamodels in the analysis of offshore systems, Yang and Zheng (2011) used polynomial regression models and Kriging models for the analysis and reliability-based optimisation of beams and steel catenary risers. Cabrera-Miranda and Paik (2018, 2017) and Cabrera-Miranda et al. (2018) employed Kriging models for predicting the loads on marine risers and mooring systems. Morató et al. (2019) also utilised Kriging models for predicting the stresses in the support structure of an OWT. Wang et al. (2020) demonstrated the use of Kriging models in the optimisation of an aeroengine high-pressure compressor blisk. The *polynomial chaos expansion* (PCE) model was used by Lim et al. (2020) for predicting the surge motion of moored floaters.

In the context of DASE, *Machine Learning* techniques constitute metamodels, in which the *artificial neural networks* (ANN) are amongst the most popular models. ANN has been successfully applied in the prediction of fatigue damage of mooring lines (Li et al., 2018; Li and Choung, 2016), estimation of burst pressure of corroded pipelines (Xu et al., 2017), analysis of cable-stayed bridge subjected to incoming loads from wind and waves (Fang et al., 2020), in the spatio-temporal prediction of waves (Law et al., 2020) and the assessment of the hull bending moment of ships in the time domain (Moreira and Guedes Soares, 2020). In this study, the *Blind Kriging* (BK) model and the feedforward ANN of the multi-layer perceptron type with backpropagation learning algorithm are the chosen candidate metamodels.

The following general form can express a metamodel as:

$$\hat{y}(\mathbf{x}) = \beta_1 B_1(\mathbf{x}) + \beta_2 B_2(\mathbf{x}) + ... + \beta_n B_n(\mathbf{x}), \tag{3}$$

where $B_1(\mathbf{x})$, $B_2(\mathbf{x})$,…, $B_n(\mathbf{x})$ are basis functions, and β_1 , β_2 ,…, β_n are coefficients inferred from the data. Moreover, $\mathbf{x}$ is the vector of input variables and the hat indicates that the metamodel $\hat{y}$ is an estimator of y.

<u>*Blind Kriging model:*</u>

Regarding the Kriging model, it requires X^{T} = [$\mathbf{x}_1$, …, $\mathbf{x}_n$] input data n (old points) and their associated outputs $\mathbf{w}$ = [$w(\mathbf{x}_1)$, …, $w(\mathbf{x}_n)$]$^{\mathrm{T}}$ = [y_1, …, y_n]$^{\mathrm{T}}$ estimated from simulations for a single response. Following several authors (Kleijnen, 2015; Morató et al., 2019; Yang and Zheng, 2011), the *Universal Kriging* (UK) model is expressed as:

$$\hat{y}_{\mathrm{UK}} = f(\mathbf{x}) + \delta(\mathbf{x}), \tag{4}$$

where $f(\mathbf{x})$ is the trend function and $\delta(\mathbf{x})$ is a zero-mean Gaussian process.

The trend function is usually expressed as a polynomial in the form of:

$$f(\mathbf{x}) = \sum_{j=1}^{L} \beta_j B_j(\mathbf{x}), \tag{5}$$

where { β_j, j =1, …, L } are the coefficients and the basis functions { $B_1(\mathbf{x})$, …, $B_L(\mathbf{x})$ } consist of polynomials that approach the mean of the output.

The Gaussian process $\delta(\mathbf{x})$ is calculated as:

$$\delta(\mathbf{x}) = \boldsymbol{\sigma}(\mathbf{x})^{\mathrm{T}} \boldsymbol{\Sigma}^{-1} (\mathbf{w} - \mu \mathbf{1}) \cong \sum_{i=1}^{n} \beta_i \rho(\mathbf{x}, \mathbf{x}_i), \tag{6}$$

where $\boldsymbol{\sigma}(\mathbf{x}) = \mathrm{cov}(y_i, y_0)$ is the vector of covariance between the old outputs $\mathbf{w}$ and the metamodel's new output $y_0(\mathbf{x})$, $\boldsymbol{\Sigma}$ denotes the $n \times n$ correlation matrix of $\mathbf{w}$, μ_Y is the Kriging parameter that comes from the estimation of the mean of the process and $\mathbf{1}$ is the all-ones vector with n entries, ρ is the correlation function between a new point $\mathbf{x}$ and an old point $\mathbf{x}_i$ that is used as the basis function in the second term, and { β_i, i =1, …, n } are the coefficients

After substitution of Eqs. (5) and (6) into (4), and selection of the polynomials of the first term by of Bayesian approximation to capture the most variance in the sample data (Couckuyt et al., 2012), the BK model can be expressed as:

$$\hat{y}_{\mathrm{BK}} = \sum_{j=1}^{L} \beta_j B_j(\mathbf{x}) + \sum_{i=1}^{n} \beta_i r(\mathbf{x}, \mathbf{x}_i). \tag{7}$$

ANN model:

In the case of the ANN model, there is a network of three layers, namely input, hidden, and output layers, that predict the output as (Fang et al., 2006):

$$\hat{y}_{\mathrm{ANN}} = \sum_{j=1}^{d} \beta_j b_j(v_j) + \beta_0, \tag{8}$$

where d is the number of synapses between the hidden layer and a neuron in the output layer, β_j is the weight connection between the output and the j-th neuron in the hidden layer, $b_j(v_j)$ is the activation function or transfer function that provides the output of the j-th neuron in the hidden layer. In turn, the linear combinations of the input variables v_j between the input and hidden layer are defined as:

$$v_j = \sum_{i=1}^{s} w_{ji} x_i + w_{j0}, \tag{9}$$

where w_{ji} is the weight connection between the j-th neuron in the hidden layer and the i-th neuron of the input layer.

After computing the metamodels, either BK model or ANN model is used based on their performance assessed by the root mean square error (RMSE), which can be calculated as

$$\text{RMSE} = \sqrt{\frac{1}{n} \sum_{i=1}^{n} \left(y_i - \hat{y}_i \right)^2}. \tag{10}$$

The RMSE is an indicator of the goodness-of-fit of the associated model (Nguyen et al., 2019). Accordingly, the metamodel with the lowest RMSE is selected for performing subsequent analyses.

2.3. Investigation of mooring layout influence

2.3.1. Numerical analysis via charts

To investigate the influence of the mooring layout on the loads, a series of response charts are employed by varying selected DVs along with the domain of interest while using metamodels to predict the loads. Additionally, charts of response divergence are used to identify regions of behaviour where loads become strongly nonlinear with respect to the inputs. The concept of divergence (Awrejcewicz et al., 2015), which is generally applied for the analysis of signals, is here modified and used to calculate the divergence between two points, which are magnitudes of loads.

The response divergence is the distance between two points, can be readily calculated by using the following formula:

$$D = |a - b|. \tag{11}$$

where a and b are responses in adjacent points while varying a parameter.

2.3.2. Sensitivity analysis of loads

The significance of the DVs and RVs influencing the hull and mooring loads is assessed here using *Sobol's sensitivity analysis* (Kleijnen, 2015). This yields a series of indexes that rank the importance of input variables. This technique has been reported to be applied in the analysis of complex engineering systems, such as land-based structures (Javidan and Kim, 2019; Xiao et al., 2017) and water resources (Kumar et al., 2020; Xu et al., 2012). In the field of ocean engineering, it has recently been applied to quantify the uncertainty in marine operations (Cheng et al., 2019).

Let us consider a random vector $\mathbf{X}=[X_1, \ldots, X_k]^{\mathrm{T}}$ and the load $Y = g(\mathbf{X})$, where $\mathbf{X}$ is made of both DVs and RVs. The *total-effect index* ($s_{j;-j}$), which measures the effect of varying X_j averaged over the variations in all the other inputs, including interaction with other variables, is defined as:

$$s_{j;-j} = 1 - \frac{Var\left[E\left(Y \mid \mathbf{X}_{-j}\right)\right]}{Var(Y)}, \tag{12}$$

where $E\left(Y \mid \mathbf{X}_{-j}\right)$ is the expected value of the response conditional to all input variables except X_j and is normalised respect to the variance of the response, here, an extreme value of a load for ULS analysis or the fatigue damage rate for FLS analysis.

A high index is indicative of a major influence on the variance of the analysed load by the uncertainty of the input variable.

3. Applied example

3.1. Target floating structure

The selection of production floating units and their mooring system is based on a number of factors such as environmental conditions of the specific sites and functional requirements. In this study, to demonstrate the applicability and effectiveness of the developed framework, we consider a hypothetical tanker-based FPSO that operates in the ultra-deep water regions of the Gulf of Mexico. The mooring system consists of the SPM type with a regular disconnection function made of 12 lines. FPSO characteristics presented in Table 1 are taken from a previous study (Cabrera-Miranda et al., 2018).

Table 1. FPSO main particulars.

Particular	**Dimension**
Length between perpendiculars	239 m
Breadth	42 m
Depth	21 m
Draft in the ballast condition	6.38 m
Draft in the fully loaded condition	15.85 m
Dead weight	108 000 t
Water depth	3 100 m

3.2. Design of simulation experiments

The probabilistic characteristics of the input DVs and RVs are presented in Table 2. To define the mooring layout, we introduce DVs X_1 through X_8 (see Fig. 2). As lower limit for the assumed uniform distributions, we have used zero, whereas the upper limit was selected such that its value surpasses the dimensions of a mooring system that was designed in a previous study (Cabrera-Miranda et al., 2018). For instance, in the former work, a layout radius (X_1) was selected with a 0.84 radius to water depth ratio, whereas in the present study, the upper limit corresponds to a ratio of 2.6. The upper value of the turret's horizontal distance respect to the CoG (X_2) was chosen to be 84% respect to the length between perpendiculars. The selected range includes typical turret positions reported in the literature (Kim et al., 2005; Milne et al., 2016; Sanchez-Mondragon et al., 2018; Tahar and Kim, 2003; Zanganeh and Thiagarajan, 2018; Zhao et al., 2013).

Regarding the number of clusters (X_3), the distribution consists of integer numbers where the 12 mooring lines could be accommodated. Moreover, the orientation of the mooring layout (X_4) is assumed uniform between $-\pi$ and π in order to account for all possibilities.

Table 2. Input variables and probabilistic characteristics.

Type	Variable	Description	Unit	Distribution	Parameters
Design variable (DV)	X_1	Layout radius	m	Uniform	From 0 to 8520
	X_2	Turret position respect to CoG	m	Uniform	From 10 to 200
	X_3	Number of clusters	-	Discrete uniform distribution	From 1 to 12 (integers only)
	X_4	Layout orientation angle	rad	Uniform	From $-\pi$ to π
	X_5	Factor of the angle between lines	-	Uniform	From 0 to 1
	X_6	Chain section diameter	m	Uniform	From 0 to 0.25
	X_7	Intermediate polyester section diameter	m	Uniform	From 0 to 0.3
	X_8	Static top-tension	N	Uniform	From 0 to 3.24×10^7
Random variable (RV)	X_9	Significant wave height (H_s)	m	Weibull	α = 1.81, β = 1.47
	X_{10}	Zero-crossing wave period (T_z)	s	Lognormal	μ = 0.7 + 0.95 $H_s^{0.158}$, σ = 0.07 + 0.1685 exp (-0.0312 H_s)
	X_{11}	Wave direction	rad	Truncated normal distribution	μ = 0, σ = 0.234, from $-\pi$ to π
	X_{12}	Wind speed (1-h average at 10 m above sea level)	$m \cdot s^{-1}$	Lognormal	μ = 0.61, σ = 0.725
	X_{13}	Wind direction	rad	Truncated normal	μ = 0, σ = 0.234, from $-\pi$ to π
	X_{14}	Current speed (surface)	$m \cdot s^{-1}$	Lognormal	μ = -1.1187, σ = 0.432
	X_{15}	Current direction	rad	Truncated normal	μ = 0, σ = 0.234, from $-\pi$ to π
	X_{16}	Draft	m	Discrete	P (6.38) = 0.4, P (15.85) = 0.6

The factor of the angle between lines (X_5) is a factor between zero and one that defines the angle between lines ϑ in the same cluster by the following expression:

$$\vartheta = (2\pi X_5) / \left[X_3 (m-1) \right], \tag{13}$$

$$m = m_T / X_3 , \tag{14}$$

where X_3 is the number of clusters, m stands for the number of lines per cluster, and m_T is the total number of lines in the mooring system, being 12 lines for this example.

Concerning the diameters for the different sections of the mooring lines, each mooring line has a bottom chain section of 150 m length by X_6 diameter, middle polyester section with a diameter of X_7, and length that is adjusted at each scenario to achieve the static top-tension (X_8). The top chain section has the same characteristics as the bottom section. The uniform distribution of the said variables were chosen such that values reported in the literature (Cabrera-Miranda et al., 2018; Kim et al., 2005; Kim and Kim, 2002; Montes-Iturrizaga et al., 2012; Tahar and Kim, 2003; Vazquez-Hernandez et al., 2006; Vázquez-Hernández et al., 2011) are included within the assumed distributions. The material properties for the mooring lines are taken from DNVGL-OS-E302 (DNV GL, 2018) and Barltrop (1998) for R4 steel grade chain and polyester rope, respectively.

It should be noted that the DVs presented in Table 2 do not represent necessarily realistic structural dimensions after a rigorous design process. Some values might be associated to a weak and unreliable mooring system, whereas others might be associated to an extremely robust system that would be expensive to implement in reality. Thus, the selection of appropriate DVs should follow a classical iterative design procedure by using the metamodels as quick estimation tools in the pre-established uniform distributions.

The RVs X_9 through X_{15} correspond to site-specific metocean conditions from the literature (Cabrera-Miranda et al., 2018; Paik, 2020). Meanwhile, X_{16} simply describes the ship's draft in fully loaded and ballast conditions.

The DASE procedure begins with the scenario sampling by LHS. To ensure that the sample size is sufficiently large to cover the sample space of inputs with adequate separation, Loeppky's rule of thumb (Kleijnen, 2017) is adopted and $n = 10k$ scenarios are selected, giving 160 scenarios sampled with LHS.

3.3. Time-domain analysis

After filtering out unfeasible scenarios, a total of 50 credible scenarios (available in Appendix B) are analysed in the time-domain with ANSYS-Aqwa (see Fig. 3). To avoid unrealistic transient response at the beginning of each motion analysis, a total of 4 hours are simulated for each scenario, out of which only the last 3 hours of time histories are further processed. Extreme ULS loads are derived as per Eq. (1) and the fatigue damage rate as per Eq. (2). Similar approaches for neglecting the transient effects are reported elsewhere (Cabrera-Miranda and Paik, 2018; Verma et al., 2019).

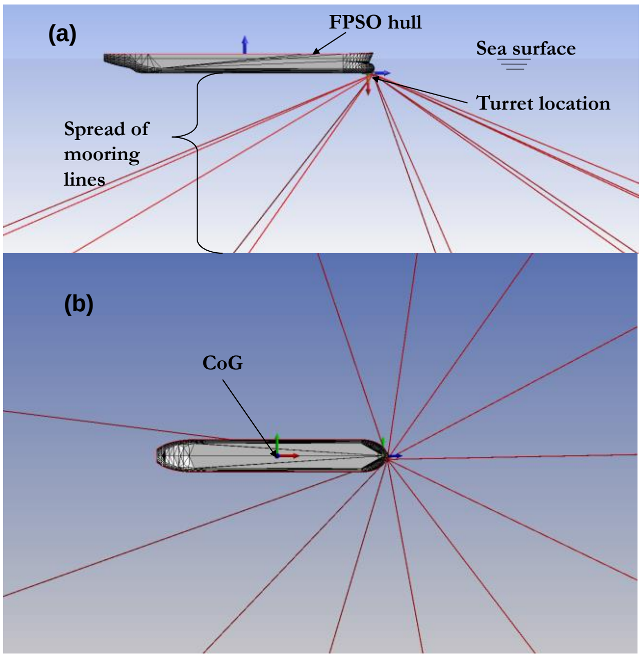

Fig. 3. An example of moored FPSO modelled in ANSYS-Aqwa.

Figure 4 presents an example of how the time-domain histories are analysed to obtain the extreme response and fatigue damage rate. One should be aware that the presented signal corresponds to a sampled scenario from the distributions in Table 2, and they are not the result of a design procedure. Figure 4(a) shows the time-domain signal of the wave-induced bending moment for 4 hours simulations; a dotted red rectangle encloses the last 3 hours of simulation out of which statistics are obtained. Figure 4(b) illustrates the PDF for the peaks of the wave-induced bending moment derived for a softening non-Gaussian process where the most probable extreme value is depicted as a yellow dot. Similarly, Figures 4(c) and (d) display the time history and peaks PDF for the tension at the top-chain section of a mooring line, respectively; the difference, respect to the response of wave-induced loads is that the said tension is essentially a hardening non-Gaussian process, which means that the tail of the PDF extends to higher values. It is observed that the adopted approach for deriving short-term extreme values is suitable for systems with nonlinear and non-Gaussian behaviours. The subfigures (e), (f) and (g) show the signal processing of the stresses at a mooring line to calculate the fatigue damage rate. Figure 4(e) shows the chain stress in the time-domain; this is then decomposed into a series of turning points as displayed in Fig. 4(f), and then, the rain-flow counting algorithm is applied for obtaining the histogram of stress range histogram in Fig. 4(g), which is then employed in Eq. (2) to calculate the fatigue damage rate.

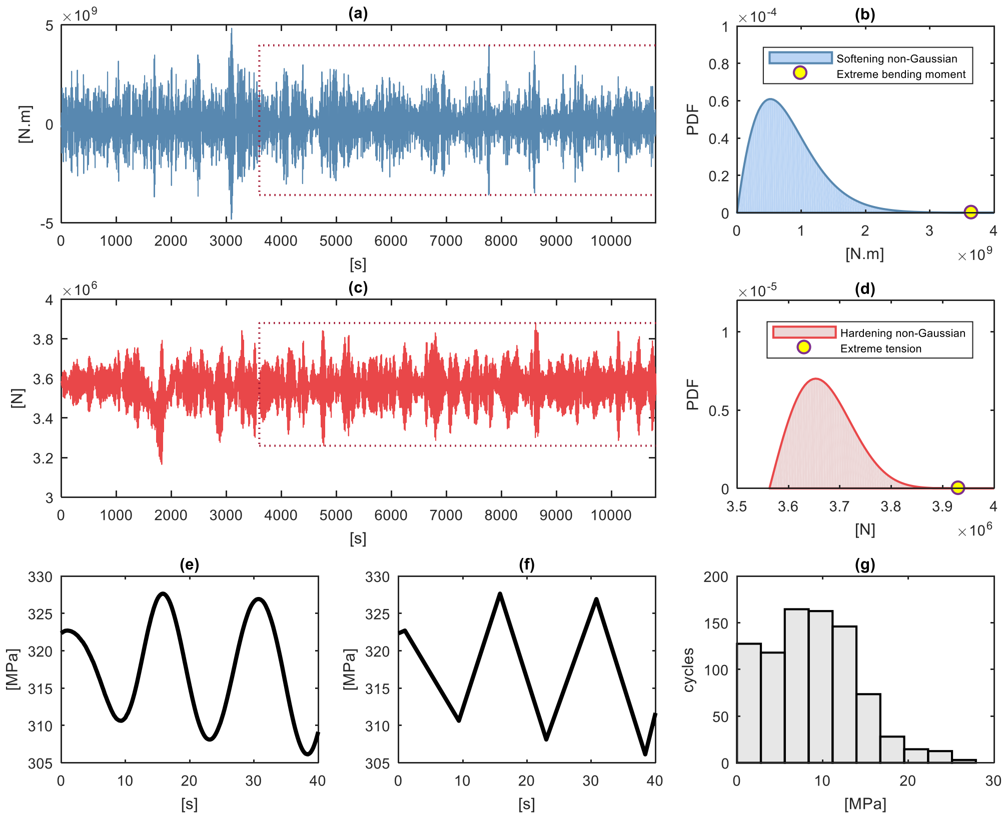

Fig. 4. An illustrative example of FPSO response (scenario 7, H_s =3.24 m, T_z =8.64 s): (a) wave-induced bending moment time history, (b) PDF of bending moment peaks, (c) tension time history at top-chain section of a mooring line, (d) PDF of tension peaks around the static tension, (e) stress time history at top chain section, (f) stress decomposition into a turning point for rainflow counting, and (g) rainflow stress range histogram. The dotted line in (a) and (c) encloses 3 hours time history used for deriving short-term extreme values and fatigue damage rate.

3.4. Metamodelling

The input and response data (X, Y) obtained from the time-domain analysis is normalised in the range of [0,1] to avoid numerical difficulties in calculations due to the magnitude difference of variables (Nguyen et al., 2019). The BK model is computed using the ooDACE Matlab toolbox (Couckuyt et al., 2012, 2010), whereas the ANN model is fitted by means of the Neural Net Fitting tool available in Matlab. Concerning the ANN, it consists of a multi-layer perceptron feedforward network with Bayesian regularisation backpropagation. The default network layout is employed, consisting of a tan-sigmoid activation function in the hidden layer and a linear activation function in the output layer. Furthermore, 30 hidden neurons were chosen after a parametric study.

Next, the metamodels' performance is assessed. Figure 5 shows the RMSE of the candidate models, for which the following nomenclature is introduced. The M_w is used to denote the short-term extreme wave-induced vertical bending moment, T stands for the short-term extreme mooring line tension, and d is fatigue damage rate. Moreover, the first two digits indicate the number of the mooring line. The digit after the hyphen indicates the analysed point at that mooring line, viz., 1 for the anchor connection, 2 for the highest point of the bottom chain section, 3 for the highest point of the polyester section and 4 for the highest point of the top chain section.

Regarding the calculation of the RMSE, this performance indicator is based on testing data for the ANN model, which follows a partition of data in subsets of 70%, 15%, and 15% for training, validating, and testing, respectively. Meanwhile, the RMSE for the BK model was estimated by applying the leave-one-out approach (Kleijnen, 2017). One should note that responses *d*-01-3, *d*-01-4, *d*-02-3, *d*-01-4, …, *d*-12-4 could be more accurately predicted by the BK model than by the ANN model; nevertheless, for the sake of simplicity at coding and in particular for efficient handling of indexes of the models, we have adopted the ANN for calculating both the ULS loads and FLS loads throughout this paper. Figure 6 illustrates the architecture of the selected model, where n_1, …, n_{30} stand for the neurons at the hidden layer.

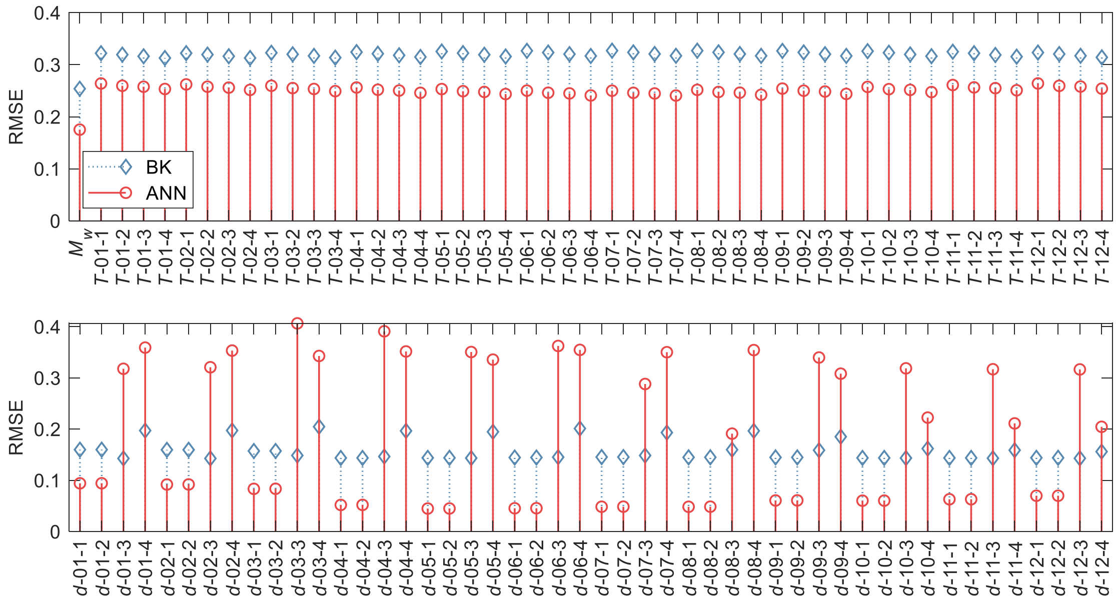

Fig. 5. Performance of the BK model and ANN model for predicting extreme loads (up) and fatigue damage rate (down). Low RMSE indicates the excellent performance of the metamodel.

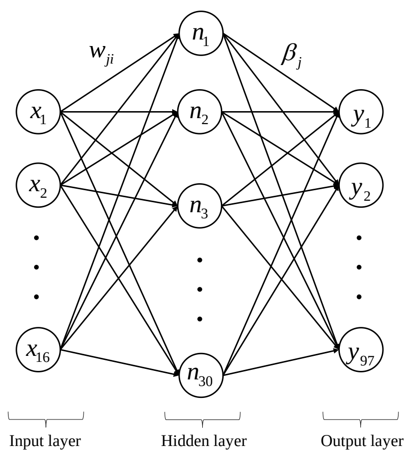

Fig. 6. Architecture of selected ANN model.

4. Results and discussions

4.1. Influence of mooring layout on the loads

4.1.1. Probabilistic selection of mooring layouts

To predict the effect of different mooring layouts on the loads, we generated six layouts using LHS. Table 3 summarises the fixed values of DVs, where x_2* represents the turret position normalised with respect to the length between perpendiculars.

Table 3. Selected mooring layouts for numerical study.

DV	Description	Unit	A	B	C	D	E	F
x_1	Layout radius	m	5727.36	8449.46	1597.45	749.61	6934.67	5091.03
x_2*	Normalised turret position	m	0.80	0.43	0.58	0.19	0.52	0.72
x_3	Number of clusters	-	3	1	3	4	12	6
x_4	Layout orientation angle	rad	-0.580	-0.196	-1.611	0.409	-2.547	2.039
x_5	Factor of angle between lines	-	0.15	0.39	0.08	0.86	0.66	0.94
x_6	Chain section diameter	m	0.009	0.188	0.026	0.164	0.120	0.209
x_7	Intermediate polyester section diameter	m	0.209	0.121	0.154	0.023	0.064	0.164
x_8	Static top-tension	N	2.89×10^7	1.92×10^7	0.70×10^7	0.15×10^7	2.50×10^7	1.46×10^7

A 3-D illustration of selected six layouts (denoted by A, B, C, D, E, and F) is shown in Fig. 7, and their qualitative description is as follows:

- *Layout A*: midsize layout radius, external turret, anchors grouped in a tight position within the clusters, very thin steel chain at the bottom and top sections, thick polyester rope at the intermediate section, and high static top-tension.
- *Layout B*: broad layout radius, turret located in ship's mid-position, the arrangement of lines is asymmetrical because all lines grouped in one region of the radius in a single cluster, the chain has a medium-size diameter as well as the polyester rope, and medium static top-tension.
- *Layout C*: narrow layout radius, turret located at the bow, tight clusters, thin chain, midsize polyester rope, and low static top-tension.
- *Layout D:* narrow radius mooring arrangement, internal turret, scattered clusters, midsize chain, thin polyester rope, and low static top-tension.
- *Layout E:* midsize layout radius, mid-position turret, scattered clusters, midsize chain, thin polyester rope, and high static top-tension.
- *Layout F:* midsize layout radius, external turret, numerous tight clusters, thick chain, midsize polyester rope, and medium static top-tension.

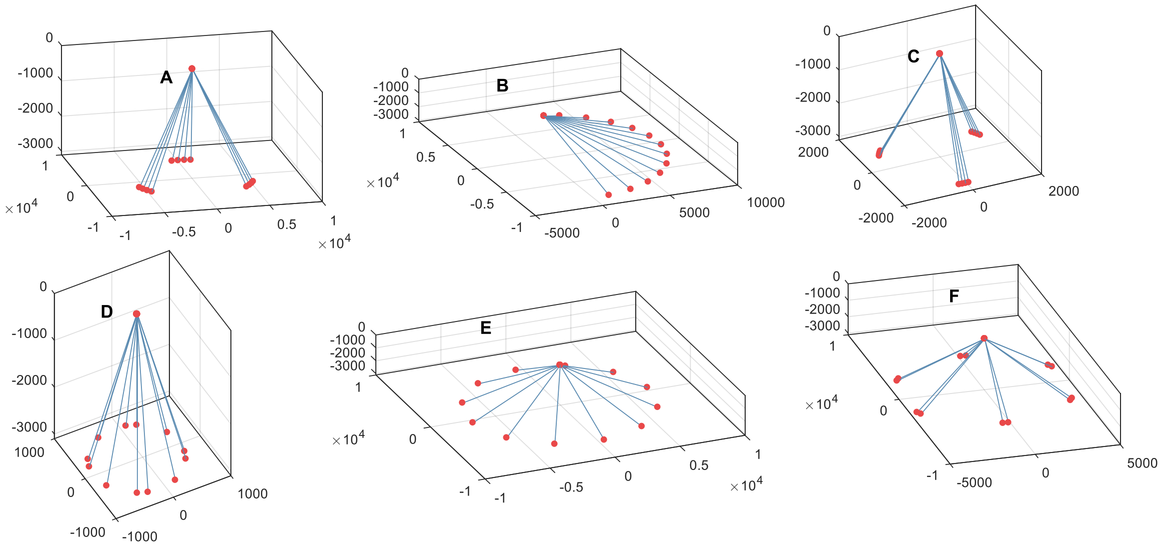

Fig. 7. Illustration of selected mooring layouts for numerical study (all coordinates are in m).

4.1.2. Load response and response divergence charts

A parametric study is conducted to investigate the response of the mooring lines against different environmental loads. The loads for the selected mooring scenarios are estimated using the developed ANN model described in Section 3.4. Accordingly, for each scenario, extreme values of three load types are measured, namely still water bending moment, tension at the top-chain section of mooring line [for a representative mooring line (line 4)], and fatigue damage rate for the same line but at the connection of the bottom chain section with the anchor. The loads at the polyester section are not presented here because the tension is not as high as for the top-chain section. In addition, fatigue damage is not presented because of the good performance of polyester against cracks. We should mention that mooring lines tensions and mooring lines fatigue damage were cut to a minimum value of zero to avoid predicting unrealistic loads by the ANN models.

In this study, we investigate the effect of varying sea wave parameters H_s and T_z on a mesh of 400×400 discrete points, whilst other RVs are fixed to their mean value. Figures 8 to 13 depict the constructed charts of the predicted loads for six mooring layouts, where the top and bottom rows represent load response and its divergence, respectively. The subfigures (a), (b), and (c) indicate extreme loads, i.e., wave-induced bending moment [N·m], tension at top-chain section of a line [N], and fatigue damage rate at the anchor connection [per year], respectively, while (d), (e), and (f) represent their respective divergence.

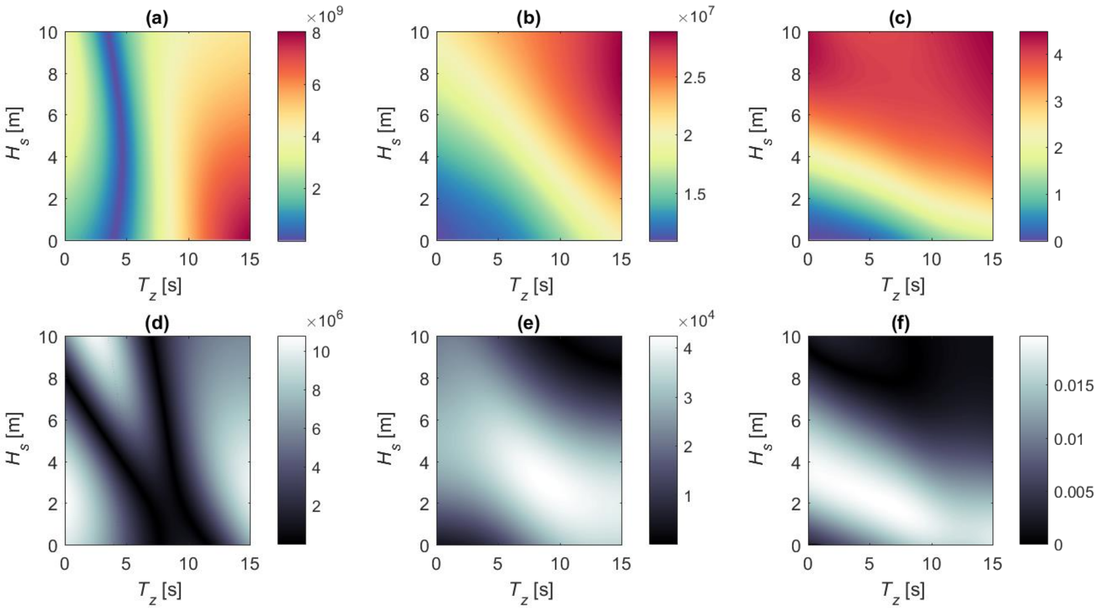

Fig. 8. Charts of response (upper row) and response divergence (lower row) for mooring case A.

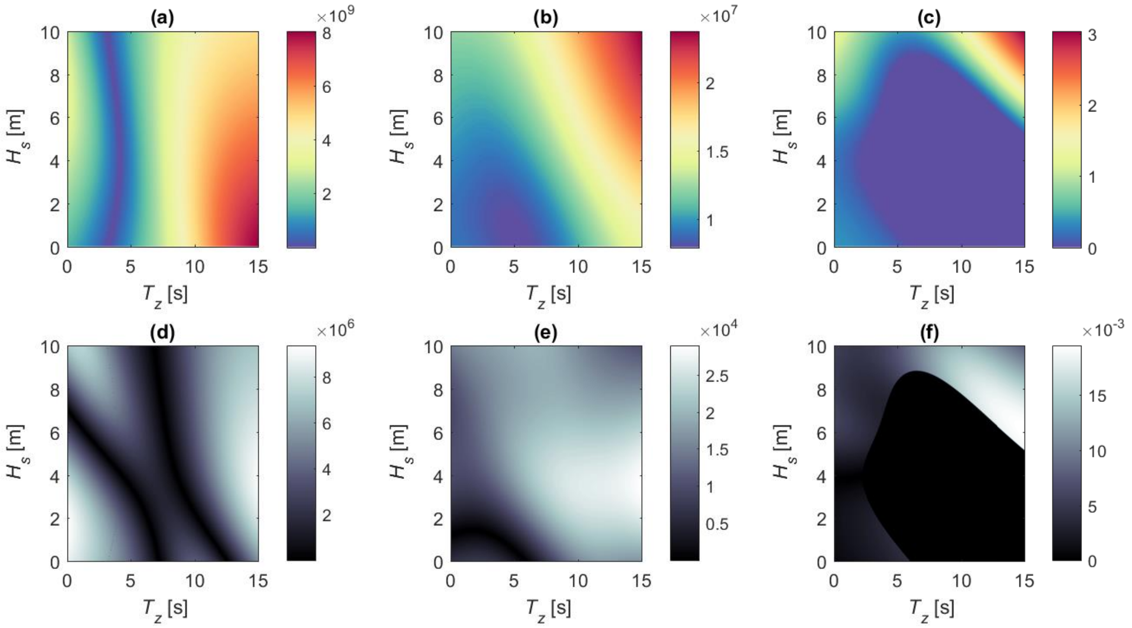

Fig. 9. Charts of response (upper row) and response divergence (lower row) for mooring case B.

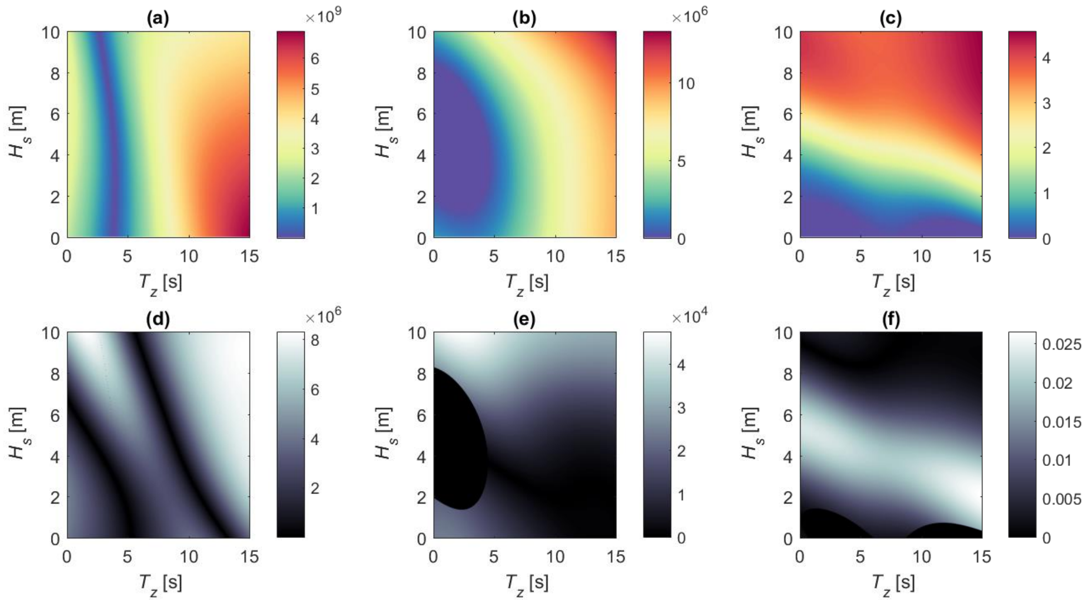

Fig. 10. Charts of response (upper row) and response divergence (lower row) for mooring case C.

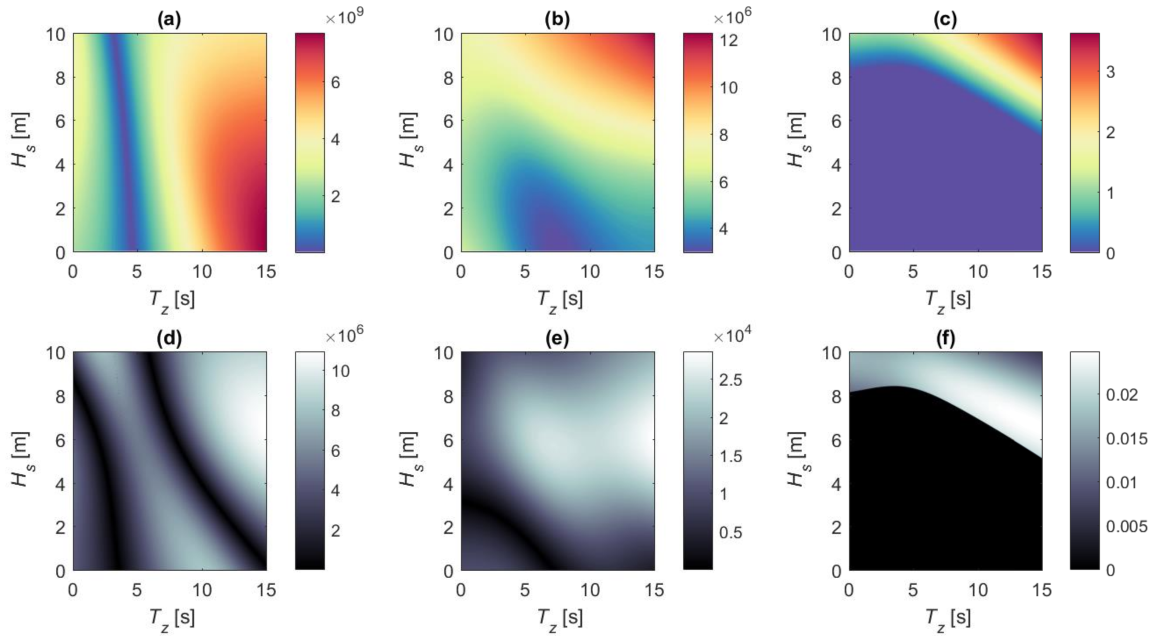

Fig. 11. Charts of response (upper row) and response divergence (lower row) for mooring case D.

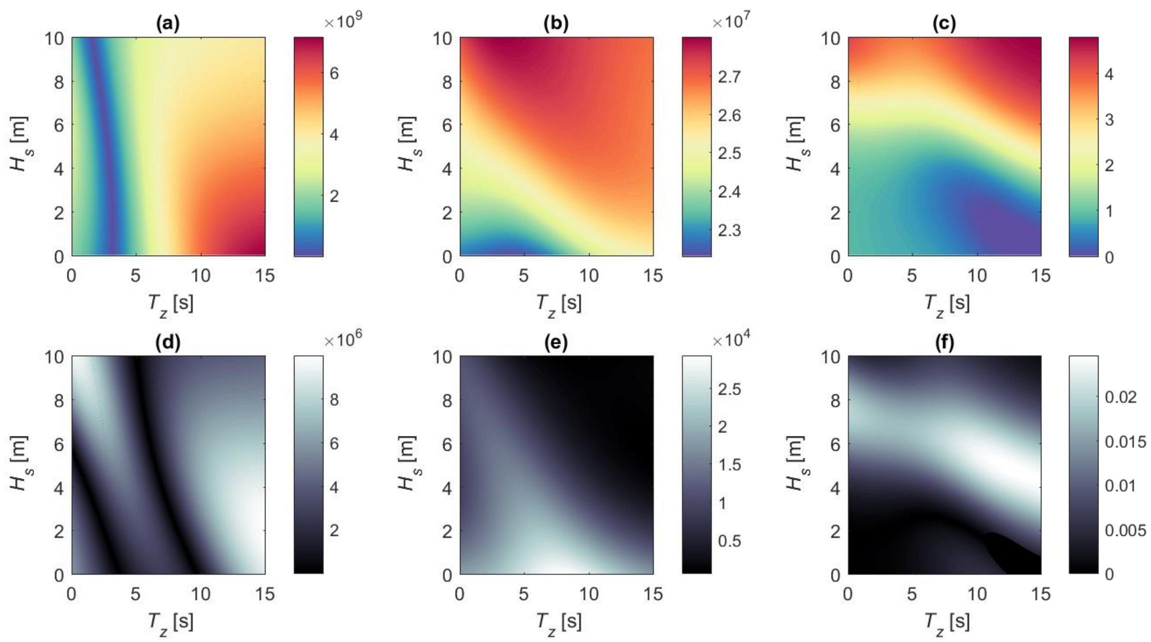

Fig. 12. Charts of response (upper row) and response divergence (lower row) for mooring case E.

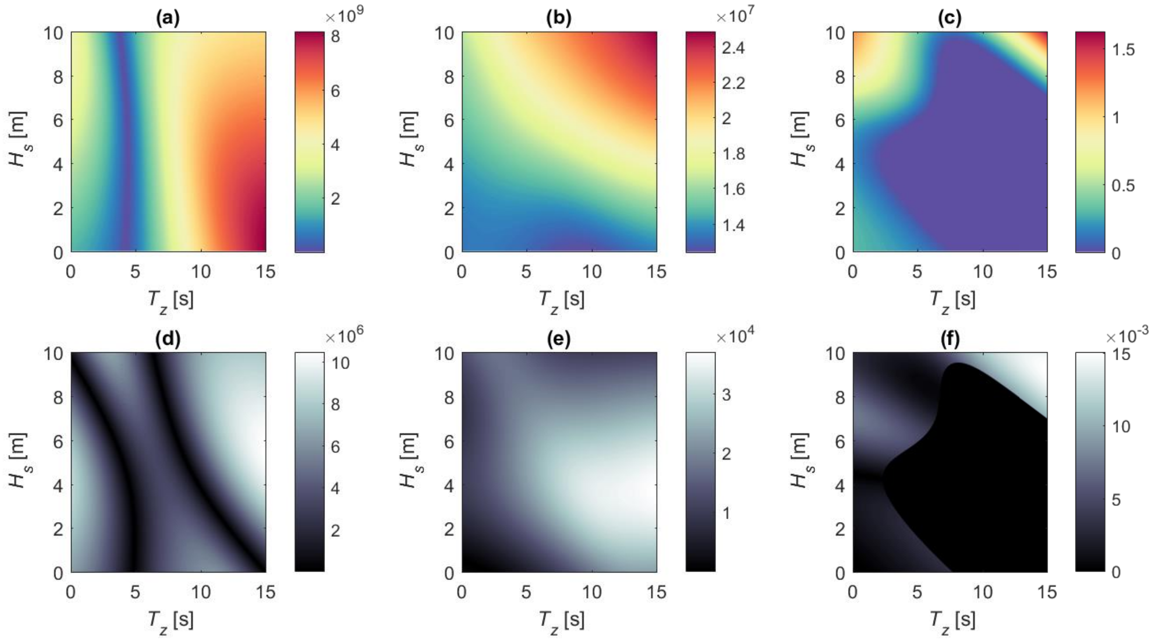

Fig. 13. Charts of response (upper row) and response divergence (lower row) for mooring case F.

Influence on hull wave-induced bending moment:

In general, all the response and response divergence charts show a similar trend for the hull loads [see Figs. 8 through 13 (a) and (d)]. The wave-induced vertical bending moments seem not to be affected significantly by the mooring layout. Further, the response charts show that peak bending moment is observed in the zone having higher T_z and lower H_s.

In the response divergence charts, black zones with low divergence and white zones with high divergence indicate highly linear and nonlinear behaviours, respectively. For all the layouts, high divergence is observed for low and high extreme combinations of H_s and T_z. In between, two bands of low divergence are observed, for instance, at T_z = 6 s and 11 s for layout A in Fig. 8(d), which bend towards lower values of T_z as H_s increases. For layout E in Fig. 12(d), the low divergence bands start at T_z = 4 s and 10 s for low H_s, which is due to the wide radius of the mooring layout that provides high lateral stiffness, reducing the natural period of the system.

We should mention that the charts in Figs. 8 to 13 have a parametric study character that shows the predicted loads by the ANN models. One should be aware that some sea states would not be presented under realistic conditions. As a result of the wave-breaking process, some combinations of H_s and T_z are more frequent, as can be observed in the wave scatter plot in Fig. 14, generated with the distributions in Table 2.

Having Fig. 14 under consideration, the magnitude of the wave-induced vertical bending moment at upper right corner of subfigure (a) in Figs. 8 to 13 is of interest. In particular, lower loads in the said sector are observed for cases A and E in Figs. 8 and 12, respectively, where the moment is in the order of 4×10^9 N·m. These layouts share the characteristics of mid-size radius and high static top-tension, parameters that are associated with the lateral stiffness of the moored-floater dynamic system.

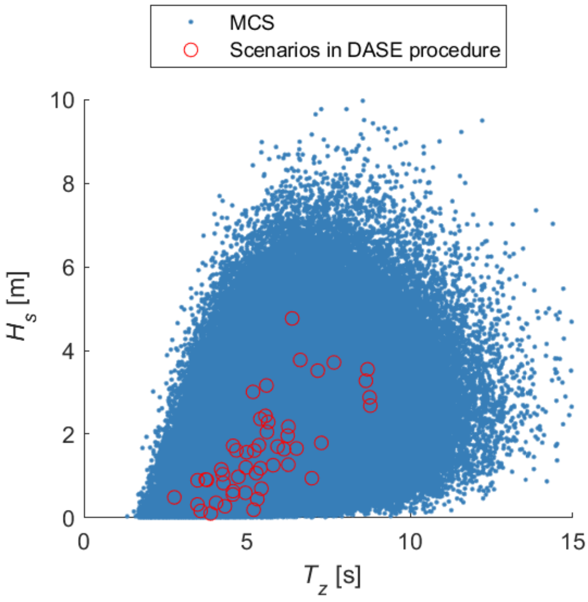

Fig. 14. Scatter plot of irregular wave characteristics after 10^6 MCS samples. Red circles show the data points used to compute the metamodels.

Influence on mooring line tension:

The results are displayed in Figs. 8 to 13, subfigures (b) and (e). A consistent increase in the tension can be observed with the increase of H_s and T_z. The magnitude of the tension is the highest for layouts A and E in Figs. 8(b) and 12(b), respectively, which are layouts of high top-tension. As for the divergence charts, low divergence is observed for low values of T_z and H_s; an exception is layout E in Fig. 12(e), where the high divergence zone is observed for intermediate values of T_z and low divergence occurs for high T_z and H_s values. A marked black shadow of low divergence can be observed in Figs. 10(e), which is due to the inaccuracy of the ANN in that particular case that would predict negative tension in that zone, and which calculation was approximated to zero tension.

Looking at the upper right corner in subfigures (b) in Figs. 8 to 13, and comparing with Table 3, it becomes evident that the maximum magnitude for the mooring line tension is strongly correlated with static top-tension. Cases with the highest tension are A and E, in Figs. 8 and 12, respectively, where the maximum tension is in the order of 2.8×10^{7} N. Given that the mooring tension is dominated by the static top-tension component, it reasonable to make early design decisions based on the static configuration, after which nonlinear time-domain analysis should of course be conducted in order to confirm the sufficiency of the mooring system. The case A in Fig. 8 is particularly critical, since the chain diameter is low, and thus, the structural reliability of the mooring system could be a concern. This should be confirmed by means of a formal reliability analysis to be conducted in a future study.

Influence on fatigue damage:

Figures 8 to 13, subfigures (c) and (f) show the results for the fatigue damage rate of the mooring at the anchor connection where fatigue could be an issue. The response charts in subfigures (c) indicate that the fatigue damage is mostly influenced by the height of the waves. Wide zones of zero fatigue damage can be observed for layout D in Fig. 11(c) and layout F in Fig. 13(c), which can be partially attributed to the medium or high diameter of the steel chain. The response divergence charts are different for each case. Figure 8(f) for layout A shows high divergence for a straight band that extends between H_s = 3.8 m and T_z = 10 s. Figure 9(f) for layout B displays a black shadow in a wide area of the chart which is due to the inadequacy of the ANN model for predicting the loads in such an asymmetrical line arrangement. In Fig. 10(f) for layout C, a band of high divergence is experienced for H_s =

5.5 m and extends towards lower values as T_z rises. A zone of high divergence is detected in Fig. 12(f) for layout E with H_s = 4 m and high T_z.

In general, zones of fatigue damage rate higher than one per year can be seen for a harsh environment, which fortunately, does not occur in the location of interest as illustrated in Fig. 14. Instead, one should focus on sea states with high density. By taking the median for the wave parameters, i.e. H_s = 1.41 m and T_z = 5.45 s, the fatigue damage rate is null for cases B, D and F in subfigures (c) of Figs. 9, 11 and 13, respectively. For the rest of the cases, namely A, C and E, the fatigue damage rate at the anchor connection is 1.06, 0.25 and 0.62 per year in Figs. 8, 10 and 12, respectively. It is noted that those values are unacceptable, because in less than four years, the three layouts might have fatigue issues.

On the basis of the results reported in Figs. 8 to 13, and with reference to Table 3 and Fig. 7, we have illustrated the dependence of the FPSO loads to the control parameters H_s and T_z related to the amplitude and period of the environmental excitation. In particular, subfigures (d), (e) and (f) indicate regions of rapid change in the response by varying the amplitude of the excitation for the same period, thus demonstrating the nonlinear nature of the system. In short, cases A and E in Figs. 8 and 12 are favourable for the hull loads, nonetheless, the tension could be excessive, resulting in too high ULS and FLS loads for the mooring lines, making these options unfeasible. Neither case C in Fig. 10 is feasible owing to its high fatigue damage rate. Moreover, case B in Fig. 9 might be unsuitable due to its low omnidirectional capabilities. The left alternatives, namely D and F in Figs. 11 and 13, seem not to share specific features in Table 3, but the only thing that can be said is that the static top-tension is not too high. It seems that the static top-tension is an important variable that must be selected high enough to keep the floater in place, but low enough to reduce the mooring ULS and FLS loads. Furthermore, low static top-tension might be desirable for the ease of installation, where the suitable installation vessel must deliver enough thrust to achieve and sustain the target tension [see for instance Webb and Van Vugt (2017)].

4.2. Sobol's sensitivity analysis

To rank the influence of input variables and identify the critical ones, we conduct Sobol's sensitivity analysis. Here, we use 10^3 samples by LHS in an outer loop and 10^4 samples by MCS in the inner loop. Furthermore, indexes with negative values were rounded up to zero since the indexes are positive by definition.

Table 4 lists the calculated total-effect index of the ULS and FLS loads, following the same nomenclature used for Fig. 5 (see Section 3.4). A total of 1552 indexes were generated, which correspond to 97 load variables (rows) and 16 input variables (columns) (see description in Table 2). The first row reports the indexes for the wave-induced bending moment (M_w). The following 48 rows list the indexes for the tension (T) of 12 mooring lines and 4 analysed points each. The last 48 rows show the indexes for the fatigue damage (d) for the same points at the mooring lines. For the sake of clarity, indexes for representative responses are presented graphically in Fig. 15. Table 4 shows that the sum of total-effect indexes in each row is greater than 1, which means that 2^{nd} order and higher interactions are counted towards the index of each input variable.

Table 4. Sobol's total-effect indexes showing the influence of uncertainty of input variables onto the variance of the loads.

	X_1	X_2	X_3	X_4	X_5	X_6	X_7	X_8	X_9	X_{10}	X_{11}	X_{12}	X_{13}	X_{14}	X_{15}	X_{16}
M_w	0.00	0.00	0.00	0.00	0.04	0.04	0.00	0.10	0.15	0.58	0.02	0.00	0.05	0.00	0.01	0.26
T-01-1	0.03	0.09	0.06	0.01	0.07	0.09	0.03	0.78	0.03	0.02	0.00	0.04	0.00	0.03	0.07	0.13
T-01-2	0.04	0.10	0.06	0.02	0.08	0.08	0.03	0.77	0.03	0.02	0.00	0.04	0.00	0.03	0.07	0.13
T-01-3	0.04	0.10	0.06	0.02	0.08	0.09	0.04	0.77	0.03	0.02	0.01	0.04	0.00	0.04	0.07	0.13
T-01-4	0.04	0.10	0.07	0.02	0.09	0.08	0.05	0.77	0.03	0.02	0.01	0.04	0.00	0.04	0.07	0.14
T-02-1	0.04	0.09	0.06	0.01	0.08	0.09	0.03	0.78	0.03	0.02	0.00	0.04	0.00	0.03	0.06	0.13
T-02-2	0.04	0.10	0.06	0.02	0.08	0.08	0.03	0.78	0.03	0.02	0.00	0.04	0.00	0.03	0.06	0.13
T-02-3	0.04	0.10	0.06	0.02	0.09	0.09	0.04	0.77	0.03	0.02	0.00	0.04	0.00	0.04	0.07	0.13
T-02-4	0.04	0.10	0.07	0.02	0.09	0.08	0.05	0.77	0.03	0.02	0.01	0.04	0.00	0.04	0.07	0.14
T-03-1	0.04	0.09	0.05	0.01	0.08	0.09	0.03	0.78	0.03	0.02	0.00	0.04	0.00	0.03	0.06	0.12
T-03-2	0.04	0.10	0.06	0.02	0.09	0.08	0.03	0.78	0.03	0.02	0.00	0.03	0.00	0.03	0.06	0.13
T-03-3	0.04	0.10	0.06	0.02	0.09	0.09	0.04	0.77	0.03	0.02	0.01	0.04	0.00	0.03	0.06	0.13
T-03-4	0.04	0.10	0.07	0.02	0.10	0.08	0.05	0.77	0.03	0.02	0.01	0.04	0.00	0.04	0.06	0.13
T-04-1	0.04	0.09	0.05	0.02	0.09	0.09	0.03	0.78	0.03	0.03	0.00	0.03	0.00	0.03	0.05	0.12
T-04-2	0.03	0.10	0.06	0.02	0.09	0.09	0.03	0.78	0.03	0.03	0.00	0.03	0.00	0.03	0.05	0.13
T-04-3	0.03	0.10	0.06	0.02	0.10	0.09	0.05	0.77	0.03	0.02	0.01	0.03	0.00	0.03	0.05	0.13
T-04-4	0.03	0.10	0.07	0.02	0.10	0.08	0.05	0.77	0.03	0.02	0.01	0.03	0.00	0.03	0.06	0.13
T-05-1	0.03	0.09	0.06	0.02	0.09	0.09	0.03	0.79	0.03	0.03	0.00	0.03	0.00	0.02	0.04	0.12
T-05-2	0.03	0.10	0.06	0.02	0.10	0.09	0.04	0.78	0.03	0.03	0.01	0.03	0.00	0.02	0.05	0.12
T-05-3	0.03	0.10	0.06	0.03	0.10	0.09	0.05	0.77	0.03	0.03	0.01	0.03	0.00	0.03	0.05	0.13
T-05-4	0.03	0.10	0.07	0.03	0.10	0.09	0.05	0.77	0.04	0.02	0.02	0.03	0.00	0.03	0.05	0.13

Table 4. Continued (1).

	X_1	X_2	X_3	X_4	X_5	X_6	X_7	X_8	X_9	X_{10}	X_{11}	X_{12}	X_{13}	X_{14}	X_{15}	X_{16}
T-06-1	0.03	0.09	0.06	0.02	0.09	0.09	0.03	0.78	0.03	0.03	0.00	0.03	0.00	0.02	0.04	0.12
T-06-2	0.03	0.10	0.06	0.03	0.10	0.09	0.04	0.78	0.03	0.03	0.01	0.03	0.00	0.02	0.04	0.12
T-06-3	0.03	0.09	0.06	0.03	0.10	0.09	0.05	0.77	0.04	0.03	0.01	0.03	0.00	0.03	0.05	0.12
T-06-4	0.03	0.10	0.07	0.03	0.10	0.09	0.05	0.77	0.04	0.03	0.02	0.03	0.00	0.03	0.05	0.13
T-07-1	0.03	0.09	0.05	0.02	0.09	0.09	0.03	0.79	0.03	0.03	0.00	0.03	0.00	0.02	0.04	0.12
T-07-2	0.03	0.10	0.06	0.03	0.10	0.09	0.04	0.78	0.03	0.03	0.01	0.03	0.00	0.02	0.04	0.12
T-07-3	0.03	0.09	0.06	0.03	0.10	0.09	0.05	0.77	0.04	0.03	0.01	0.03	0.00	0.03	0.05	0.12
T-07-4	0.03	0.10	0.07	0.03	0.10	0.09	0.05	0.77	0.04	0.02	0.02	0.03	0.00	0.03	0.05	0.13
T-08-1	0.03	0.09	0.05	0.02	0.09	0.09	0.03	0.79	0.03	0.03	0.00	0.03	0.00	0.02	0.04	0.12
T-08-2	0.03	0.10	0.06	0.02	0.09	0.09	0.04	0.78	0.03	0.03	0.00	0.03	0.00	0.02	0.05	0.12
T-08-3	0.03	0.10	0.06	0.03	0.10	0.09	0.05	0.77	0.03	0.02	0.01	0.04	0.00	0.03	0.05	0.12
T-08-4	0.03	0.10	0.07	0.03	0.10	0.09	0.05	0.77	0.04	0.02	0.01	0.03	0.00	0.03	0.05	0.13
T-09-1	0.03	0.09	0.05	0.02	0.08	0.09	0.03	0.79	0.03	0.03	0.00	0.03	0.00	0.02	0.05	0.12
T-09-2	0.03	0.10	0.06	0.02	0.09	0.09	0.03	0.78	0.03	0.02	0.00	0.03	0.00	0.02	0.05	0.12
T-09-3	0.03	0.10	0.06	0.02	0.09	0.09	0.05	0.77	0.03	0.02	0.01	0.04	0.00	0.03	0.06	0.13
T-09-4	0.03	0.10	0.07	0.02	0.09	0.09	0.05	0.77	0.03	0.02	0.01	0.04	0.00	0.03	0.06	0.13
T-10-1	0.03	0.09	0.05	0.02	0.08	0.09	0.03	0.78	0.03	0.02	0.00	0.04	0.00	0.03	0.06	0.12
T-10-2	0.03	0.10	0.06	0.02	0.08	0.09	0.03	0.78	0.03	0.02	0.00	0.04	0.00	0.03	0.06	0.13
T-10-3	0.03	0.10	0.06	0.02	0.09	0.09	0.04	0.77	0.03	0.02	0.01	0.04	0.00	0.03	0.06	0.13
T-10-4	0.03	0.10	0.07	0.02	0.09	0.09	0.05	0.77	0.03	0.02	0.01	0.04	0.00	0.03	0.06	0.13

Table 4. Continued (2).

	X_1	X_2	X_3	X_4	X_5	X_6	X_7	X_8	X_9	X_{10}	X_{11}	X_{12}	X_{13}	X_{14}	X_{15}	X_{16}
T-11-1	0.03	0.09	0.05	0.01	0.07	0.09	0.03	0.78	0.03	0.02	0.00	0.04	0.00	0.03	0.06	0.12
T-11-2	0.03	0.10	0.06	0.02	0.08	0.09	0.03	0.78	0.03	0.02	0.00	0.04	0.00	0.03	0.07	0.13
T-11-3	0.03	0.10	0.06	0.02	0.08	0.09	0.04	0.77	0.03	0.02	0.00	0.04	0.00	0.03	0.07	0.13
T-11-4	0.03	0.10	0.07	0.02	0.09	0.09	0.05	0.77	0.03	0.02	0.01	0.04	0.00	0.04	0.07	0.14
T-12-1	0.03	0.09	0.06	0.01	0.07	0.09	0.03	0.78	0.03	0.02	0.00	0.04	0.00	0.03	0.07	0.13
T-12-2	0.03	0.10	0.06	0.02	0.08	0.09	0.03	0.77	0.03	0.02	0.00	0.04	0.00	0.03	0.07	0.13
T-12-3	0.03	0.10	0.06	0.02	0.08	0.09	0.04	0.77	0.03	0.02	0.00	0.04	0.00	0.04	0.07	0.13
T-12-4	0.03	0.10	0.07	0.02	0.09	0.09	0.05	0.77	0.03	0.02	0.01	0.04	0.00	0.04	0.07	0.14
d-01-1	0.01	0.22	0.30	0.05	0.04	0.56	0.18	0.13	0.21	0.01	0.30	0.04	0.15	0.30	0.17	0.22
d-01-2	0.01	0.22	0.30	0.05	0.04	0.56	0.18	0.13	0.21	0.01	0.30	0.04	0.15	0.30	0.17	0.22
d-01-3	0.00	0.01	0.00	0.00	0.29	0.43	0.00	0.34	0.24	0.04	0.00	0.00	0.00	0.00	0.14	0.06
d-01-4	0.05	0.21	0.28	0.08	0.06	0.58	0.13	0.12	0.20	0.02	0.29	0.05	0.16	0.27	0.16	0.21
d-02-1	0.01	0.22	0.31	0.04	0.04	0.55	0.19	0.13	0.21	0.01	0.30	0.04	0.15	0.31	0.17	0.22
d-02-2	0.01	0.22	0.31	0.04	0.04	0.55	0.19	0.13	0.21	0.01	0.30	0.04	0.15	0.31	0.17	0.22
d-02-3	0.00	0.02	0.00	0.00	0.29	0.43	0.00	0.33	0.25	0.03	0.00	0.00	0.00	0.00	0.14	0.06
d-02-4	0.04	0.21	0.29	0.07	0.06	0.57	0.15	0.13	0.20	0.02	0.29	0.05	0.16	0.28	0.16	0.21
d-03-1	0.02	0.22	0.34	0.04	0.02	0.55	0.21	0.14	0.21	0.01	0.30	0.05	0.15	0.32	0.19	0.23
d-03-2	0.02	0.22	0.34	0.04	0.02	0.55	0.21	0.14	0.21	0.01	0.30	0.05	0.15	0.32	0.19	0.23
d-03-3	0.00	0.11	0.00	0.00	0.20	0.45	0.00	0.20	0.33	0.12	0.08	0.00	0.00	0.00	0.06	0.00
d-03-4	0.04	0.21	0.34	0.05	0.03	0.57	0.19	0.13	0.20	0.02	0.30	0.06	0.15	0.31	0.17	0.22

Table 4. Continued (3).

	X_1	X_2	X_3	X_4	X_5	X_6	X_7	X_8	X_9	X_{10}	X_{11}	X_{12}	X_{13}	X_{14}	X_{15}	X_{16}
d-04-1	0.18	0.26	0.59	0.10	0.00	0.57	0.29	0.18	0.12	0.03	0.35	0.11	0.16	0.35	0.28	0.26
d-04-2	0.18	0.26	0.59	0.10	0.00	0.57	0.29	0.18	0.12	0.03	0.35	0.11	0.16	0.35	0.28	0.26
d-04-3	0.48	0.21	0.01	0.00	0.37	0.16	0.19	0.00	0.33	0.31	0.08	0.08	0.06	0.11	0.00	0.11
d-04-4	0.22	0.26	0.62	0.12	0.00	0.57	0.30	0.19	0.10	0.04	0.34	0.13	0.16	0.35	0.27	0.25
d-05-1	0.19	0.25	0.60	0.10	0.00	0.57	0.29	0.17	0.13	0.04	0.34	0.10	0.15	0.36	0.28	0.26
d-05-2	0.19	0.25	0.60	0.10	0.00	0.57	0.29	0.17	0.13	0.04	0.34	0.10	0.15	0.36	0.28	0.26
d-05-3	0.50	0.20	0.01	0.00	0.40	0.14	0.19	0.00	0.31	0.30	0.07	0.07	0.07	0.14	0.00	0.13
d-05-4	0.23	0.25	0.63	0.12	0.00	0.58	0.30	0.16	0.11	0.05	0.32	0.11	0.15	0.36	0.28	0.24
d-06-1	0.19	0.25	0.59	0.11	0.00	0.57	0.29	0.16	0.13	0.04	0.33	0.09	0.15	0.36	0.28	0.26
d-06-2	0.19	0.25	0.59	0.11	0.00	0.57	0.29	0.16	0.13	0.04	0.33	0.09	0.15	0.36	0.28	0.26
d-06-3	0.48	0.21	0.01	0.00	0.38	0.15	0.19	0.00	0.32	0.31	0.08	0.07	0.07	0.12	0.00	0.11
d-06-4	0.23	0.25	0.63	0.12	0.00	0.58	0.29	0.15	0.11	0.05	0.31	0.09	0.14	0.36	0.28	0.23
d-07-1	0.16	0.25	0.56	0.10	0.00	0.57	0.28	0.15	0.15	0.03	0.34	0.08	0.15	0.36	0.27	0.26
d-07-2	0.16	0.25	0.56	0.10	0.00	0.57	0.28	0.15	0.15	0.03	0.34	0.08	0.15	0.36	0.27	0.26
d-07-3	0.50	0.19	0.01	0.00	0.39	0.14	0.17	0.00	0.31	0.30	0.07	0.07	0.08	0.13	0.00	0.10
d-07-4	0.18	0.24	0.57	0.11	0.00	0.58	0.27	0.13	0.14	0.04	0.31	0.06	0.13	0.36	0.26	0.24
d-08-1	0.15	0.26	0.56	0.10	0.00	0.57	0.28	0.17	0.15	0.03	0.35	0.09	0.16	0.35	0.28	0.26
d-08-2	0.15	0.26	0.56	0.09	0.00	0.57	0.28	0.17	0.15	0.03	0.35	0.09	0.16	0.35	0.28	0.26
d-08-3	0.00	0.21	0.00	0.05	0.27	0.47	0.00	0.10	0.27	0.36	0.11	0.05	0.00	0.00	0.07	0.00
d-08-4	0.17	0.25	0.58	0.11	0.00	0.57	0.28	0.16	0.14	0.03	0.34	0.09	0.15	0.36	0.28	0.25

Table 4. Continued (4).

	X_1	X_2	X_3	X_4	X_5	X_6	X_7	X_8	X_9	X_{10}	X_{11}	X_{12}	X_{13}	X_{14}	X_{15}	X_{16}
d-09-1	0.16	0.26	0.57	0.10	0.00	0.56	0.28	0.18	0.14	0.03	0.35	0.11	0.16	0.35	0.28	0.27
d-09-2	0.16	0.26	0.57	0.09	0.00	0.56	0.28	0.18	0.14	0.03	0.35	0.11	0.16	0.35	0.28	0.27
d-09-3	0.00	0.07	0.00	0.00	0.18	0.25	0.00	0.26	0.26	0.24	0.16	0.00	0.00	0.00	0.11	0.09
d-09-4	0.18	0.27	0.59	0.10	0.00	0.57	0.29	0.19	0.13	0.03	0.35	0.12	0.16	0.35	0.28	0.26
d-10-1	0.19	0.27	0.61	0.11	0.00	0.56	0.29	0.19	0.13	0.03	0.36	0.12	0.16	0.35	0.29	0.27
d-10-2	0.19	0.27	0.60	0.11	0.00	0.56	0.29	0.19	0.13	0.03	0.36	0.12	0.16	0.35	0.29	0.27
d-10-3	0.00	0.04	0.00	0.00	0.28	0.43	0.00	0.32	0.24	0.10	0.00	0.00	0.00	0.00	0.13	0.04
d-10-4	0.22	0.28	0.64	0.12	0.00	0.57	0.31	0.21	0.11	0.03	0.36	0.14	0.17	0.35	0.29	0.26
d-11-1	0.19	0.26	0.60	0.11	0.00	0.57	0.29	0.19	0.13	0.03	0.36	0.12	0.16	0.35	0.29	0.27
d-11-2	0.19	0.26	0.60	0.11	0.00	0.57	0.28	0.19	0.13	0.03	0.36	0.12	0.16	0.35	0.29	0.27
d-11-3	0.00	0.03	0.00	0.00	0.29	0.44	0.00	0.32	0.24	0.08	0.00	0.00	0.00	0.00	0.13	0.04
d-11-4	0.23	0.27	0.63	0.13	0.00	0.57	0.29	0.21	0.10	0.03	0.36	0.14	0.17	0.34	0.28	0.26
d-12-1	0.19	0.26	0.58	0.12	0.00	0.57	0.27	0.19	0.12	0.02	0.36	0.11	0.16	0.34	0.27	0.26
d-12-2	0.19	0.26	0.58	0.12	0.00	0.57	0.27	0.19	0.12	0.02	0.36	0.11	0.16	0.34	0.27	0.26
d-12-3	0.00	0.03	0.00	0.00	0.30	0.44	0.00	0.33	0.24	0.08	0.00	0.00	0.00	0.00	0.13	0.04
d-12-4	0.23	0.25	0.60	0.15	0.00	0.59	0.25	0.21	0.09	0.03	0.36	0.13	0.17	0.32	0.26	0.25

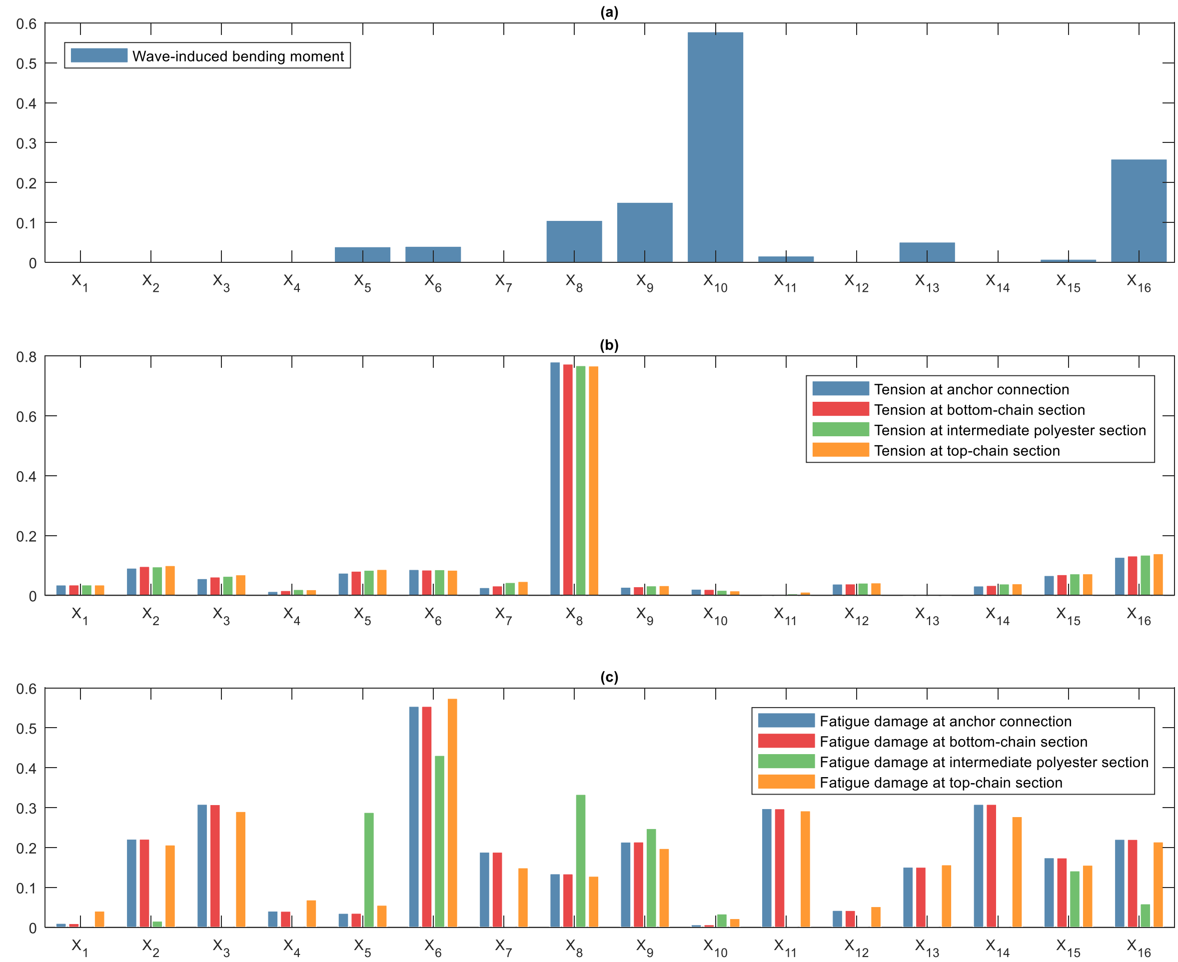

Fig. 15. Distribution of total-effect indexes for the FPSO loads: (a) wave-induced bending moment [N·m], (b) tension at a representative mooring line [N], and (c) fatigue damage rate at a representative mooring line [year^{-1}].

Figure 15(a) shows that the wave-induced bending moment (M_w) is highly influenced by the zero-crossing wave period of the waves (X_{10}) and vessel's draft (X_{16}). The results illustrate that the factor of the angle between lines (X_5) and the chain diameter (X_6) are the

DVs with the greatest influence on the wave-induced bending moment. This information should preferably be interpreted together with the correlation coefficients, which are presented in Table 5. For instance, the variables X_5 and X_6 have positive and negative correlation coefficients with the wave-induced bending moment, respectively. It can be concluded that the wave loads on the hull are dominated by environmental conditions, and thus, little can be done to influence those loads through design decisions.

Table 5. Matrix of correlation coefficients.

	X_2	X_3	X_5	X_6	X_8	M_w	*T*-02-4	*d*-02-1 (chain)	*d*-02-3 (polyester)
X_2	1.000	0.012	0.005	-0.007	-0.002	-0.124	-0.183	-0.239	0.075
X_3	0.012	1.000	0.002	-0.004	0.006	0.176	0.163	0.350	0.075
X_5	0.005	0.002	1.000	0.005	0.003	0.025	0.197	-0.038	-0.198
X_6	-0.007	-0.004	0.005	1.000	0.005	-0.141	0.001	-0.410	-0.340
X_8	-0.002	0.006	0.003	0.005	1.000	-0.039	0.851	0.041	-0.270
M_w	-0.124	0.176	0.025	-0.141	-0.039	1.000	0.064	0.374	0.425
T-02-4	-0.183	0.163	0.197	0.001	0.851	0.064	1.000	0.186	-0.237
d-02-1 (chain)	-0.239	0.350	-0.038	-0.410	0.041	0.374	0.186	1.000	0.224
d-02-3 (polyester)	0.075	0.075	-0.198	-0.340	-0.270	0.425	-0.237	0.224	1.000

Concerning the response of mooring line tension [see Fig. 15(b) and Table 4 (rows *T*-02-1 to *T*-02-4)], the total-effect indexes follow similar trends for each of the analysed points in the mooring line. Among the DVs, the indexes for static top-tension (X_8) are the highest by a big margin, for instance, of 0.69 respect to the turret position respect to CoG (X_2) for *T*-02-1, and a margin of 0.67 also respect to X_2 for *T*-02-4. Furthermore, X_8 holds positive correlation respect to the mooring line tension as seen in Table 5. The DVs X_2 and chain diameter (X_6) are the ones with the second highest influence. It can be noticed that X_2 has negative correlation coefficient, suggesting that the ULS loads are lower for a turret located close to the CoG. As for the RVs, the vessel's draft (X_{16}) is the one with highest influence, having a total-effect index of 0.14 for the top-chain section and 0.13 for the other mooring line sections. The highest total-effect indexes for ULS mooring loads correspond to DVs, accordingly, the lines' tensions can be influenced at the design stage and their variance do not strongly depend on the uncertainty of the marine environment.

Results for the fatigue damage rate are presented in Table 4 (rows *d*-02-1 to *d*-02-4) and Fig. 15(c). The total effect-indexes of fatigue damage rate at the anchor point in Table 4, row *d*-02-1 indicate that the chain diameter (X_6) has the largest influence with negative correlation, as shown in Table 5. The indexes show equal influence by the number of clusters (X_3) and current speed (X_{14}). Next input variables with major influence can be ranked as: wave direction (X_{11}), turret position (X_2), draft (X_{16}), significant wave height (X_9), polyester section diameter (X_7), current direction (X_{15}), wind direction (X_{13}), static top-tension (X_8), layout orientation (X_4), angle between lines of the same cluster (X_5), wind speed (X_{12}), layout radius (X_1) and zero-crossing wave period (X_{10}). The order of the indexes remains the same for the fatigue damage rate for other chain sections, including the top point at the mooring chain bottom (see Table 4, row *d*-02-2) and the highest point top-chain section (see Table 4, row *d*-02-4); however, the characteristics are slightly changed for the polyester rope section in Table 4, *d*-02-3.

For the fatigue damage rate at the top point at the polyester section, the chain diameter (X_6) is dominant but with a lower total-effect index than for the chain sections, followed by the top-tension (X_8) with a negative correlation (see Table 5). Other input variables can be ranked in order of importance for the fatigue damage at the polyester section as angle between lines of the same cluster (X_5), significant wave height (X_9), draft (X_{16}), zero-crossing wave period (X_{10}) and turret position (X_2). Because the polyester ropes are not susceptible to failure by fatigue, the indexes associated to several variables show negligible influence on the variance, such as the layout radius (X_1), number of clusters (X_3), layout orientation angle (X_4), polyester rope diameter (X_7), wave direction (X_{11}), wind speed (X_{12}), current speed (X_{15}) and current direction (X_{16}). Overall, the total-effect indexes for the fatigue damage rate show that the uncertainty in the variables associated with the sea current, namely current speed and direction, have a predominant influence on the variance of the fatigue damage at the chain sections. Therefore, it is advised that fatigue analysis of taut SPM systems in deep water should be conducted in the time-domain in order to account for the effect of current.

To conclude, the results of Sobol's sensitivity analysis have shown that both DVs and RVs exert influence on loads of the ship-shaped offshore installation. The wave-induced bending moment is mostly influenced by RVs; nevertheless, there are a few DVs with significant indexes, suggesting that there is room for improving the hydrodynamic performance of the hull by adjusting the parameters associated with the mooring lines. Considering the variance of the mooring ULS loads, the static top-tension should be adjusted to keep the vessel in position while not consuming a significant portion of the line's strength. Thus, the chain and polyester rope diameters should be carefully selected. Finally, the chain diameter introduces the greatest uncertainty into the fatigue damage at the chain section. Besides, the current speed and direction have an important contribution to the variance of the fatigue damage.

5. Conclusions

This work investigated the loads on ship-shaped offshore installations for hull ULS, mooring lines ULS and mooring lines FLS. It aims to find how the parameters that define the mooring layout, such as layout radius, number of clusters and diameter, influence the said loads. For this purpose, a DASE procedure has been followed. It starts by sampling credible scenarios by LHS, which are then analysed in the time-domain to obtain the moored floater loads. With the generated data, metamodels are computed, out of which ANN models are chosen to predict the loads owing to its good performance. The developed procedure is demonstrated using a hypothetical FPSO installed in the ultra-deep water regions of the Gulf of Mexico. Furthermore, because the resulting ANN models have been computed considering the uncertainties, they can be used as rapid estimation tools of loads during the design phase of mooring systems, such as parametric studies, reliability-based design, and reliability-based design optimisation.

The paper proposes the use of charts response charts that allow investigating the loads as a function of amplitude and period of irregular sea waves. Compared to the regular framework, the parametric study here conducted permits not only to quantify a response as function of changing parameters, but it also allows to characterise the nonlinear behaviour of the moored floating structure by means of divergence charts. In addition, the proposed framework introduces the utilisation of Sobol's sensitivity analysis to rank input variables according to their variance-based importance in association to each load. The use of the proposed methodology has proved useful in expanding the understanding of how the variables that define a mooring layout influence the loads. Furthermore, because neither divergence charts nor Sobol's sensitivity analysis have been applied to the analysis of moored floating structures hitherto, this study adds to the existing techniques.

The calculated total-effect indexes show that the wave-induced bending moment is highly influenced by the angle between the lines of the same cluster and by the chain diameter at the top and bottom section of the mooring lines. The ULS loads for the mooring lines are influenced by the static top-tension and the turret location respect to the CoG. In contrast, the fatigue damage is affected by the chain diameter and arrangement of clusters.

The results of this research offer useful insight into the variables that deserve more attention at the design stage of a mooring system. Of course, one must exercise care in not generalising these findings as the relationships are nonlinear and are strongly dependent on the interactions with other variables. Given that design guidelines cannot still be established, further research is needed in mooring layouts, for which the authors recommend investigating the influence of the mooring layout in the structural reliability, including Accidental Limit States (ALS) and the life-cycle costs of the ship-shaped offshore structures. In particular, the authors are interested in using ANN models in the prediction of loads on a ship-shaped offshore installation and using them in the development of reliability-based design optimisation procedures that can aid engineers in the safe design of marine structures. Further improvement of the metamodels's performance is suggested by refinement of the ANN architecture, use of other training algorithms, and even use of other metamodels types, such as deep learning models.

CREdiT authorship contribution statement

M.P. Mujeeb-Ahmed: methodology; formal analysis; investigation; data curation; writing - review & editing. **José Cabrera:** conceptualization; methodology; software; resources; data curation; writing - original draft. **Hyeong Jin Kim:** software; formal analysis; writing -

review & editing. **Jeom Kee Paik:** validation; resources; writing - review & editing; supervision.

Acknowledgements

We are indebted to Prof Wilson Guachamin-Acero at Escuela Politécnica Nacional (EPN) for his in-depth discussion on the time-domain hydrodynamic analysis of floating structures. Furthermore, we are grateful to all the researchers cited in this paper.

Funding

This research did not receive any specific grant from funding agencies in the public, commercial, or not-for-profit sectors.

Appendix A. Peak factors for non-Gaussian loads

Given that the peak factors available in the literature have been derived separately for softening and hardening non-Gaussian process, the following piece-wise function can be used:

$$g_{NG} = \begin{cases} g_S, & \gamma_4 \geq 3 \\ g_H, & \gamma_4 < 3 \end{cases} \tag{A1}$$

Let us define the load factor for a Gaussian process as

$$G = \sqrt{2\ln\left[\nu_Y^+\left(\mu_Y\right)\tau\right]}, \tag{A2}$$

which, after being multiplied by σ_Y is transformed from the standard Gaussian space into a non-standard Gaussian space, becoming the most probable extreme value (Naess and Moan, 2013).

For a softening non-Gaussian process, the thick tail of the probabilistic distribution results in milder extreme values than for a Gaussian process. A suitable expression can be found by transforming G in the standard Gaussian space into the standard non-Gaussian space by using the moment-based Hermite model for softening non-Gaussian processes (Ding and Xinzhong, 2016; Hao and Yang, 2020). Hence, the peak factor can be written as:

$$g_S = \kappa\left[G + h_3\left(G^2 - 1\right) + h_4\left(G^3 - 3G\right)\right],$$

$$\kappa = 1\Big/\sqrt{1+2h_3^2+6_4^2},\ h_3 = \left(\gamma_3/6\right)\left\{\left(1-0.015\left|\gamma_3\right| + 0.3\gamma_3{}^2\right)\Big/\left[1+0.2\left(\gamma_4-3\right)\right]\right\},$$

$$h_4 = h_{40}\left[1-1.43\gamma_3^2/\left(\gamma_4-3\right)\right]^{1-0.1\gamma_4^{0.8}},\ h_{40} = \left(1/10\right)\left\{\left[1+1.25\left(\gamma_4-3\right)\right]^{1/3} - 1\right\}. \qquad \text{(A3)}$$

On the contrary, for a hardening non-Gaussian process, the tail extends to higher extreme values. The peak factor g_H can be found by solving the following moment-based translation model equation for a hardening non-Gaussian process (Ding and Xinzhong, 2016):

$$G = h_1 + h_2 g_H - h_3\left(g_H{}^2 - 1\right) - h_4\left(g_H^3 - 3g_H\right),$$

$$b_2 = \varphi\left\{1-\left(\gamma_3^4 + 1.2\gamma_3^2 - 0.18\right)\Big/\left[7.5\exp\left(0.5\gamma_4\right)\right]\right\},$$

$$b_3 = -\left(0.8\gamma_3^5 + \gamma_3^3 + 0.77\gamma_3\right)\Big/\left[\left(\gamma_4 - 1\right)^2 + 0.5\right],$$

$$b_4 = -\varphi\left\{0.04 - \left(11.5\gamma_3^4 + 6.8\gamma_3^2 + 3.5\right)\Big/\left[\left(\gamma_4^2 + 0.4\right)^2 + 0.15\right]\right\},$$

$$\varphi = \left[1 - 0.06\left(3 - \gamma_4\right)\right]^{1/3},\ h_1 = -b_4\gamma_3,\ h_2 = b_2 - b_3\gamma_3 - b_4\gamma_4 + 3b_4,$$

$$h_3 = -b_3,\ h_4 = -b_4. \tag{A4}$$

Appendix B. Scenarios for station-keeping analysis

Table B.1. Fifty scenarios selected using LHS for time-domain analysis.

Scenario	X_1 (m)	X_2 (m)	X_3	X_4 (rad)	X_5	X_6 (m)	X_7 (m)	X_8 ($\times 10^7$) (N)	X_9 (m)	X_{10} (s)	X_{11} (rad)	X_{12} ($m \cdot s^{-1}$)	X_{13} (rad)	X_{14} ($m \cdot s^{-1}$)	X_{15} (rad)	X_{16} (m)
1	4998.3	83.7	3	-1.329	0.251	0.055	0.234	0.483	3.01	5.183	0.445	1.17	-0.082	0.67	0.142	15.85
2	1133.4	140.4	2	-1.614	0.149	0.152	0.275	0.058	0.98	4.733	-0.240	1.50	-0.230	0.27	0.063	15.85
3	8172.8	66.7	6	-0.375	0.784	0.094	0.084	0.893	1.66	6.519	0.260	1.24	-0.189	0.36	0.119	15.85
4	8219.7	36.8	6	2.411	0.215	0.062	0.128	1.323	1.18	5.411	-0.391	1.05	0.160	0.39	-0.168	6.83
5	2875.3	69.1	2	-3.089	0.598	0.079	0.247	0.558	1.72	4.574	-0.068	1.22	-0.162	0.27	0.096	6.83
6	8471.2	144.6	3	1.607	0.526	0.070	0.113	0.266	2.88	8.761	0.235	4.68	-0.060	0.24	-0.120	15.85
7	7766.1	134.3	4	-0.569	0.079	0.084	0.152	0.308	3.27	8.644	0.460	0.90	0.080	0.34	0.044	15.85
8	3609.6	162.6	12	-2.170	0.546	0.223	0.186	3.054	0.16	3.580	-0.272	0.87	-0.218	0.40	-0.190	15.85
9	7596.2	124.6	12	2.144	0.325	0.246	0.188	0.293	2.18	6.270	0.147	3.97	0.174	0.47	-0.202	15.85
10	2126.3	14.4	3	-1.282	0.485	0.175	0.179	0.348	0.70	5.441	-0.236	6.24	-0.074	0.20	-0.068	15.85
11	6305.6	71.2	12	2.228	0.445	0.247	0.211	3.196	3.52	7.169	-0.054	1.81	0.392	0.35	-0.210	15.85
12	3008.4	18.8	3	1.176	0.225	0.224	0.269	1.485	2.36	5.410	0.093	2.94	-0.170	0.51	0.202	15.85
13	3471.0	105.7	6	-1.171	0.368	0.101	0.230	0.335	0.45	5.316	0.406	4.04	0.478	0.32	-0.247	15.85
14	5616.0	158.0	4	1.669	0.696	0.098	0.238	0.737	2.05	5.610	0.060	2.56	-0.183	0.48	0.023	15.85
15	5116.8	159.0	6	2.895	0.420	0.128	0.213	2.112	3.16	5.596	-0.012	0.72	-0.086	0.34	-0.407	6.83
16	6566.9	97.9	1	1.317	0.101	0.058	0.242	2.041	2.29	5.649	0.005	3.23	0.506	0.50	-0.026	15.85
17	6388.4	90.6	4	-2.738	0.856	0.162	0.185	1.460	0.56	4.569	-0.179	3.78	0.115	0.37	0.134	15.85
18	2670.8	57.6	4	3.020	0.060	0.049	0.287	2.144	3.77	6.633	-0.100	3.28	0.075	0.41	-0.348	15.85
19	8352.9	187.7	1	0.662	0.289	0.151	0.297	1.149	1.07	5.282	0.022	1.02	0.306	0.48	-0.117	6.83
20	1177.1	173.6	1	2.183	0.051	0.081	0.218	1.096	1.04	4.255	-0.128	0.69	-0.136	0.51	-0.003	15.85
21	7370.2	95.2	2	-0.464	0.138	0.032	0.105	1.906	0.10	3.888	0.277	0.49	0.264	0.30	-0.551	15.85
22	2369.1	25.1	12	-1.554	0.331	0.014	0.214	1.627	1.16	4.211	-0.165	1.64	0.022	0.12	-0.020	15.85

23	3912.6	102.8	4	-1.256	0.155	0.140	0.117	3.000	2.68	8.781	-0.104	1.61	-0.454	0.26	-0.315	15.85
24	2416.6	78.3	6	-0.296	0.375	0.054	0.174	2.452	0.19	5.203	0.247	0.84	0.430	0.17	-0.081	6.83
25	5996.0	193.6	12	-0.549	0.666	0.119	0.172	0.121	0.36	4.052	-0.217	4.91	-0.015	0.40	0.193	15.85
26	8448.8	29.3	12	-0.235	0.355	0.180	0.228	0.583	1.61	4.674	0.354	2.22	-0.025	0.24	-0.113	6.83
27	1006.0	104.2	12	0.273	0.181	0.123	0.282	0.946	2.44	5.566	-0.086	1.33	0.400	0.61	-0.046	15.85
28	3121.3	99.6	2	-1.878	0.808	0.042	0.155	1.825	0.60	4.951	0.015	3.12	-0.365	0.28	0.246	15.85
29	6602.6	44.7	1	2.675	0.846	0.221	0.092	1.452	0.27	4.324	-0.209	2.43	0.241	0.37	0.519	15.85
30	4922.2	109.8	12	-2.990	0.093	0.148	0.181	2.387	4.77	6.384	0.554	2.91	0.213	0.29	-0.224	15.85
31	5252.2	38.5	3	-2.090	0.024	0.145	0.252	1.939	3.71	7.666	-0.007	3.58	-0.205	0.93	0.007	15.85
32	1881.2	178.1	6	0.416	0.639	0.200	0.204	2.351	0.90	3.769	0.272	0.60	0.111	0.58	0.333	15.85
33	2954.7	15.5	6	0.759	0.554	0.044	0.232	2.171	1.20	4.967	0.045	17.08	0.073	0.44	-0.255	15.85
34	6181.0	49.0	2	0.848	0.635	0.173	0.158	3.121	1.61	5.224	-0.065	0.80	0.050	0.38	0.129	6.83
35	5868.4	108.5	3	-2.206	0.266	0.092	0.147	1.649	3.55	8.696	0.050	1.83	0.147	0.34	-0.270	6.83
36	1352.9	13.1	2	-2.978	0.543	0.242	0.136	0.152	1.79	7.279	-0.547	7.62	-0.071	0.17	-0.181	6.83
37	4493.9	31.4	12	0.979	0.525	0.097	0.132	1.731	1.73	5.366	0.194	1.05	-0.267	1.01	-0.053	15.85
38	6689.3	70.2	6	-1.963	0.237	0.194	0.284	1.080	0.49	2.772	-0.134	2.52	-0.252	0.19	0.187	6.83
39	888.1	28.3	2	1.789	0.954	0.109	0.285	0.773	0.94	6.988	0.313	1.58	0.055	0.14	0.017	15.85
40	3552.1	100.8	4	1.453	0.108	0.108	0.205	3.205	1.64	6.134	-0.294	2.87	0.024	0.36	0.315	15.85
41	6930.9	42.1	1	-2.659	0.942	0.105	0.115	2.233	0.91	3.734	-0.002	1.74	-0.037	0.35	-0.198	15.85
42	1454.7	26.2	3	2.800	0.853	0.184	0.201	2.846	0.64	4.569	-0.037	1.94	0.035	0.25	-0.308	6.83
43	4244.2	120.4	1	-0.424	0.963	0.201	0.102	0.382	0.32	3.482	0.027	3.73	-0.257	0.30	-0.294	6.83
44	4173.8	174.1	1	0.616	0.069	0.112	0.149	2.304	1.96	6.248	0.251	0.56	-0.021	0.29	-0.342	15.85
45	2174.0	188.3	6	2.327	0.579	0.132	0.262	0.015	1.56	4.988	0.199	0.45	-0.122	0.36	-0.196	15.85
46	4757.7	111.4	2	1.886	0.083	0.129	0.300	0.543	0.83	4.277	0.127	3.08	-0.127	0.60	-0.258	6.83
47	4840.9	109.2	12	-1.604	0.997	0.208	0.154	1.894	1.26	5.802	-0.264	8.60	0.337	0.28	0.049	6.83
48	8082.0	156.3	1	0.299	0.933	0.156	0.109	3.074	0.90	3.487	0.035	2.68	0.245	0.26	-0.231	6.83
49	1852.4	141.6	6	-1.087	0.870	0.237	0.159	0.449	1.27	6.268	-0.011	0.76	0.032	0.10	-0.132	15.85
50	4536.1	87.8	6	-3.134	0.175	0.231	0.257	2.984	1.70	5.937	-0.149	1.10	0.223	0.42	-0.036	6.83

References

ANSYS, 2020. Aqwa User's Manual. Canonsburg, USA.

Awrejcewicz, J., Krysko, A. V., Zagniboroda, N.A., Dobriyan, V. V., Krysko, V.A., 2015. On the general theory of chaotic dynamics of flexible curvilinear Euler–Bernoulli beams. Nonlinear Dyn. 79, 11–29. https://doi.org/10.1007/s11071-014-1641-5

Barltrop, N.D.P., 1998. Floating Structures: a Guide for Design and Analysis, Volume Two. CMPT/Oilfield Publications Limited, Ledbury, England.

Cabrera-Miranda, J.M., Paik, J.K., 2018. Long-term stochastic heave-induced dynamic buckling of a top-tensioned riser and its influence on the ultimate limit state reliability. Ocean Eng. 149, 156–169. https://doi.org/10.1016/j.oceaneng.2017.12.012

Cabrera-Miranda, J.M., Paik, J.K., 2017. On the probabilistic distribution of loads on a marine riser. Ocean Eng. 134, 105–118. https://doi.org/10.1016/j.oceaneng.2017.01.025

Cabrera-Miranda, J.M., Sakugawa, P.M., Corona-Tapia, R., Paik, J.K., 2018. On design criteria for a disconnectable FPSO mooring system associated with expected life-cycle cost. Ships Offshore Struct. 13, 432–442. https://doi.org/10.1080/17445302.2017.1412049

Cheng, X., Li, G., Skulstad, R., Major, P., Chen, S., Hildre, H.P., Zhang, H., 2019. Data-driven uncertainty and sensitivity analysis for ship motion modeling in offshore operations. Ocean Eng. 179, 261–272. https://doi.org/10.1016/j.oceaneng.2019.03.014

Couckuyt, I., Declercq, F., Dhaene, T., Rogier, H., Knockaert, L., 2010. Surrogate-based infill optimization applied to electromagnetic problems. Int. J. RF Microw. Comput. Eng. 20, 492–501. https://doi.org/10.1002/mmce.20455

Couckuyt, I., Forrester, A., Gorissen, D., De Turck, F., Dhaene, T., 2012. Blind Kriging: Implementation and performance analysis. Adv. Eng. Softw. 49, 1–13. https://doi.org/10.1016/j.advengsoft.2012.03.002

Ding, J., Xinzhong, C., 2016. Moment-based translation model for hardening non-Gaussian response processes. J. Eng. Mech. 142, 06015006. https://doi.org/10.1061/(asce)em.1943-7889.0000986

DNV GL, 2020. DNVGL-OS-E301 Position Mooring. Høvik, Norway.

DNV GL, 2018. DNVGL-OS-E302 Offshore mooring chain. Høvik.

Fang, C., Tang, H., Li, Y., Zhang, J., 2020. Stochastic response of a cable-stayed bridge under non-stationary winds and waves using different surrogate models. Ocean Eng. 199, 106967. https://doi.org/10.1016/j.oceaneng.2020.106967

Fang, K., Li, R.Z., Sudjianto, A., 2006. Design and modeling for computer experiments, Computer Science and Data Analysis Series. Chapman & Hall/CRC, Boca Raton, FL, USA.

Hao, W., Yang, Q., 2020. Reformative translation model for probability density functions of amplitude processes of crosswind-excited super-tall buildings. Adv. Struct. Eng. 23, 847–856. https://doi.org/10.1177/1369433219886086

Javidan, M.M., Kim, J., 2019. Variance-based global sensitivity analysis for fuzzy random structural systems. Comput. Civ. Infrastruct. Eng. 34, 602–615. https://doi.org/10.1111/mice.12436

Kim, M.H., Koo, B.J., Mercier, R.M., Ward, E.G., 2005. Vessel/mooring/riser coupled dynamic analysis of a turret-moored FPSO compared with OTRC experiment. Ocean Eng. 32, 1780–1802. https://doi.org/10.1016/j.oceaneng.2004.12.013

Kim, Y.B., Kim, M.H., 2002. Hull/Mooring/Riser Coupled Dynamic Analysis of a Tanker-Based Turret-moored FPSO in Deep Water, in: Proceedings of The Twelfth (2002) International Offshore and Polar Engineering Conference. The International Society of Offshore and Polar Engineers, Kitakyushu, Japan, pp. 169–175.

Kleijnen, J.P.C., 2017. Regression and Kriging metamodels with their experimental designs in simulation: A review. Eur. J. Oper. Res. 256, 1–16. https://doi.org/10.1016/j.ejor.2016.06.041

Kleijnen, J.P.C., 2015. Kriging Metamodels and Their Designs, in: Design and Analysis of Simulation Experiments. Springer, Cham, pp. 179–239. https://doi.org/10.1007/978-3-319-18087-8_5

Kumar, D., Singh, A., Kumar, P., Jha, R.K., Sahoo, S.K., Jha, V., 2020. Sobol sensitivity analysis for risk assessment of uranium in groundwater. Environ. Geochem. Health 42, 1789–1801. https://doi.org/10.1007/s10653-020-00522-5

Kwon, D.K., Kareem, A., 2011. Peak factors for non-Gaussian load effects revisited. J. Struct. Eng. 137, 1611–1619. https://doi.org/10.1061/(ASCE)ST.1943-541X.0000412

Law, Y.Z., Santo, H., Lim, K.Y., Chan, E.S., 2020. Deterministic wave prediction for unidirectional sea-states in real-time using Artificial Neural Network. Ocean Eng. 195. https://doi.org/10.1016/j.oceaneng.2019.106722

Li, C.B., Choung, J., 2016. Fatigue damage analysis for a floating offshore wind turbine mooring line using the artificial neural network approach. Ships Offshore Struct. 12(sup1), 1–8. https://doi.org/10.1080/17445302.2016.1254522

Li, C.B., Choung, J., Noh, M.H., 2018. Wide-banded fatigue damage evaluation of Catenary mooring lines using various Artificial Neural Networks models. Mar. Struct. 60, 186–200. https://doi.org/10.1016/j.marstruc.2018.03.013

Li, L., Jiang, Z., Ong, M.C., Hu, W., 2019. Design optimization of mooring system: An application to a vessel-shaped offshore fish farm. Eng. Struct. 197, 109363. https://doi.org/10.1016/j.engstruct.2019.109363

Lim, H., Manuel, L., Low, Y.M., 2021. On Efficient Surrogate Model Development for Prediction of the Long-Term Extreme Response of a Moored Floating Structure. J. Offshore Mech. Arct. Eng. 143, 011703. https://doi.org/10.1115/1.4047545

Liu, S., 2020. Revisiting the influence of a ship's draft on the drift force due to diffraction effect. Sh. Technol. Res. 67, 175–180. https://doi.org/10.1080/09377255.2020.1780717

Liu, S., Papanikolaou, A., 2020. Prediction of the Side Drift Force of Full Ships Advancing in Waves at Low Speeds. J. Mar. Sci. Eng. 8, 377. https://doi.org/10.3390/jmse8050377

Mathisen, J., Larsen, K., 2004. Risk-based inspection planning for mooring chain. J. Offshore Mech. Arct. Eng. 126, 250–257. https://doi.org/10.1115/1.1782644

Milne, I.A., Delaux, S., McComb, P., 2016. Validation of a predictive tool for the heading of turret-moored vessels. Ocean Eng. 128, 22–40. https://doi.org/10.1016/j.oceaneng.2016.10.007

Montes-Iturrizaga, R., Heredia-Zavoni, E., Silva-González, F., Straub, D., 2012. Nested reliability analysis of mooring lines for floating systems. Appl. Ocean Res. 34, 107–115.

https://doi.org/10.1016/j.apor.2011.09.005

Morató, A., Sriramula, S., Krishnan, N., 2019. Kriging models for aero-elastic simulations and reliability analysis of offshore wind turbine support structures. Ships Offshore Struct. 14, 545–558. https://doi.org/10.1080/17445302.2018.1522738

Moreira, L., Guedes Soares, C., 2020. Neural network model for estimation of hull bending moment and shear force of ships in waves. Ocean Eng. 206, 107347. https://doi.org/10.1016/j.oceaneng.2020.107347

Mujeeb-Ahmed, M.P., Paik, J.K., 2021. Quantitative collision risk assessment of a fixed-type offshore platform with an offshore supply vessel. Structures 29, 2139–2161. https://doi.org/10.1016/j.istruc.2020.06.026

Mujeeb-Ahmed, M.P., Paik, J.K., 2019. A probabilistic approach to determine design loads for collision between an offshore supply vessel and offshore installations. Ocean Eng. 173, 358–374. https://doi.org/10.1016/j.oceaneng.2018.12.059

Naess, A., Moan, T., 2013. Response Statistics, in: Stochastic Dynamics of Marine Structures. Cambridge University Press, Cambridge, pp. 233–251. https://doi.org/10.1017/CBO9781139021364.011

Nguyen, T., Kashani, A., Ngo, T., Bordas, S., 2019. Deep neural network with high-order neuron for the prediction of foamed concrete strength. Comput. Civ. Infrastruct. Eng. 34, 316–332. https://doi.org/10.1111/mice.12422

Niesłony, A., 2009. Determination of fragments of multiaxial service loading strongly influencing the fatigue of machine components. Mech. Syst. Signal Process. 23, 2712–2721. https://doi.org/10.1016/j.ymssp.2009.05.010

Noble Denton Europe Ltd, 2001. Rationalisation of FPSO design issues—Relative reliability levels achieved between different FPSO limit states. Health & Safety Executive, Norwich.

Ozguc, O., 2020. Conversion of an oil tanker into FPSO in Gulf of Mexico: strength and fatigue assessment. Ships Offshore Struct. https://doi.org/10.1080/17445302.2020.1790298

Paik, J.K., 2020. Computational Models for Offshore Structural Load Analysis in Collisions, in: Advanced Structural Safety Studies. Springer, Singapore, pp. 145–187. https://doi.org/10.1007/978-981-13-8245-1_7

Paik, J.K., Czujko, J., Kim, B.J., Seo, J.K., Ryu, H.S., Ha, Y.C., Janiszewski, P., Musial, B., 2011. Quantitative assessment of hydrocarbon explosion and fire risks in offshore installations. Mar. Struct. 24, 73–96. https://doi.org/10.1016/j.marstruc.2011.02.002

Paik, J.K., Lee, S.E., Kim, B.J., Seo, J.K., Ha, Y.C., Matsumoto, T., Byeon, S.H., 2015. Toward a Probabilistic Approach to Determine Nominal Values of Tank Slosing Loads in Structural Design of Liquefied Natural Gas FPSOs. J. Offshore Mech. Arct. Eng. 137, 021801. https://doi.org/10.1115/1.4029666

Paik, J.K., Thayamballi, A.K., 2007. Overview of Ship-Shaped Offshore Installations, in: Ship-Shaped Offshore Installations: Design, Building, and Operation. Cambridge University Press, Cambridge, pp. 1–30. https://doi.org/10.1017/CBO9780511546082.003

Peng, L., Liu, M., Yang, Q., Huang, G., Chen, B., 2020. An analytical formula for Gaussian to non-Gaussian correlation relationship by moment-based piecewise Hermite polynomial model with application in wind engineering. J. Wind Eng. Ind. Aerodyn. 198, 104094. https://doi.org/10.1016/j.jweia.2020.104094

Pillai, A.C., Thies, P.R., Johanning, L., 2019. Mooring system design optimization using a surrogate assisted multi-objective genetic algorithm. Eng. Optim. 51, 1370–1392. https://doi.org/10.1080/0305215X.2018.1519559

Ringsberg, J.W., Jansson, H., Ö rgård, M., Yang, S.-H., Johnson, E., 2020a. Design of Mooring Solutions and Array Systems for Point Absorbing Wave Energy Devices—Methodology and Application. J. Offshore Mech. Arct. Eng. 142, 031101. https://doi.org/10.1115/1.4045370

Ringsberg, J.W., Yang, S.-H., Lang, X., Johnson, E., Kamf, J., 2020b. Mooring forces in a floating point-absorbing WEC system – a comparison between full-scale measurements and numerical simulations. Ships Offshore Struct. 15, S70–S81. https://doi.org/10.1080/17445302.2020.1746122

Ryu, S., Duggal, A.S., Heyl, C.N., Geem, Z.W., 2016. Cost-Optimized FPSO Mooring Design Via Harmony Search. J. Offshore Mech. Arct. Eng. 138, 061303. https://doi.org/10.1115/1.4034374

Sanchez-Mondragon, J., Vázquez-Hernández, A.O., Cho, S.K., Sung, H.G., 2018. Yaw motion analysis of a FPSO turret mooring system under wave drift forces. Appl. Ocean Res. 74, 170–187. https://doi.org/10.1016/j.apor.2018.02.013

Schut, X., Dam, M., 2016. Mooring optimization in time domain using harmony search, in: Offshore Technology Conference. Houston, Texas, USA, OTC-26978-MS. https://doi.org/10.4043/26978-ms

Sengupta, B., Ahmad, S., 1996. Reliability assessment of tension leg platform tethers under nonlinearly coupled loading. Reliab. Eng. Syst. Saf. 53, 47–60. https://doi.org/10.1016/0951-8320(96)00016-6

Seo, J.K., Kim, D.C., Ha, Y.C., Kim, B.J., Paik, J.K., 2013. A methodology for determining efficient gas detector locations on offshore installations. Ships Offshore Struct. 8, 524–535. https://doi.org/10.1080/17445302.2012.713219

Shafieefar, M., Rezvani, A., 2007. Mooring optimization of floating platforms using a genetic algorithm. Ocean Eng. 34, 1413–1421. https://doi.org/10.1016/j.oceaneng.2006.10.005

Shields, M.D., Zhang, J., 2016. The generalization of Latin hypercube sampling. Reliab. Eng. Syst. Saf. 148, 96–108. https://doi.org/10.1016/j.ress.2015.12.002

Stanisic, D., Efthymiou, M., Kimiaei, M., Zhao, W., 2018. Design loads and long term distribution of mooring line response of a large weathervaning vessel in a tropical cyclone environment. Mar. Struct. 61, 361–380. https://doi.org/10.1016/j.marstruc.2018.06.004

Stanisic, D., Efthymiou, M., White, D.J., Kimiaei, M., 2019. Mooring system reliability in tropical cyclone and North Sea winter storm environments. Appl. Ocean Res. 88, 306–316. https://doi.org/10.1016/j.apor.2019.05.004

Tahar, A., Kim, M.H., 2003. Hull/mooring/riser coupled dynamic analysis and sensitivity study of a tanker-based FPSO. Appl. Ocean Res. 25, 367–382. https://doi.org/10.1016/j.apor.2003.02.001

Tang, W., Zhuang, H., Tang, Z., Guo, S., Yan, F., 2020. Mooring positioning performance of jack-up platform. Ships Offshore Struct. 15, 633–644. https://doi.org/10.1080/17445302.2019.1663657

Thiagarajan, K.P., Finch, S., 1999. An investigation into the effect of turret mooring location on the vertical motions of an FPSO vessel. J. Offshore Mech. Arct. Eng. 121, 71–76. https://doi.org/10.1115/1.2830080

Vazquez-Hernandez, A.O., Ellwanger, G.B., Sagrilo, L.V.S., 2006. Reliability-based comparative study for mooring lines design criteria. Appl. Ocean Res. 28, 398–406. https://doi.org/10.1016/j.apor.2007.05.004

Vázquez-Hernández, A.O., Ellwanger, G.B., Sagrilo, L.V.S., 2011. Long-term response analysis of FPSO mooring systems. Appl. Ocean Res. J. 33, 375–383. https://doi.org/10.1016/j.apor.2011.05.003

Verma, A.S., Jiang, Z., Vedvik, N.P., Gao, Z., Ren, Z., 2019. Impact assessment of a wind turbine blade root during an offshore mating process. Eng. Struct. 180, 205–222. https://doi.org/10.1016/j.engstruct.2018.11.012

Wang, Y.Z., Zheng, X.Y., Lu, C., Zhu, S.P., 2020. Structural dynamic probabilistic evaluation using a surrogate model and genetic algorithm. Proc. Inst. Civ. Eng. Marit. Eng. 173, 13–27. https://doi.org/10.1680/jmaen.2019.28

Webb, C.M., Van Vugt, M., 2017. Offshore construction - Installing the world’s deepest FPSO development, in: Offshore Technology Conference. Houston, Texas, USA, OTC-27655-MS. https://doi.org/10.4043/27655-ms

Xiao, S., Lu, Z., Qin, F., 2017. Estimation of the Generalized Sobol’s Sensitivity Index for Multivariate Output Model Using Unscented Transformation. J. Struct. Eng. 143, 06016005. https://doi.org/10.1061/(asce)st.1943-541x.0001721

Xie, Z.T., Yang, J.M., Hu, Z.Q., Zhao, W.H., Zhao, J.R., 2015. The horizontal stability of an

FLNG with different turret locations. Int. J. Nav. Archit. Ocean Eng. 7, 244–258. https://doi.org/10.1515/ijnaoe-2015-0017

Xu, J., Shu, H., Jiang, H., Dong, L., 2012. Sobol' sensitivity analysis of parameters in the common land model for simulation of water and energy fluxes. Earth Sci. Informatics 5, 167–179. https://doi.org/10.1007/s12145-012-0105-z

Xu, W.-Z., Li, C.B., Choung, J., Lee, J.-M., 2017. Corroded pipeline failure analysis using artificial neural network scheme. Adv. Eng. Softw. 112, 255–266. https://doi.org/10.1016/j.advengsoft.2017.05.006

Yan, J., Qiao, D., Ou, J., 2018. Optimal design and hydrodynamic response analysis of deep water mooring system with submerged buoys. Ships Offshore Struct. 13, 476–487. https://doi.org/10.1080/17445302.2018.1426282

Yang, H.Z., Zheng, W., 2011. Metamodel approach for reliability-based design optimization of a steel catenary riser. J. Mar. Sci. Technol. 16, 202–213. https://doi.org/10.1007/s00773-011-0121-6

Yang, S.-H., Ringsberg, J.W., Johnson, E., Hu, Z., 2020. Experimental and numerical investigation of a taut-moored wave energy converter: a validation of simulated mooring line forces. Ships Offshore Struct. 15, S55–S69. https://doi.org/10.1080/17445302.2020.1772667

Yang, S.-H., Ringsberg, J.W., Johnson, E., Hu, Z., Bergdahl, L., Duan, F., 2018. Experimental and numerical investigation of a taut-moored wave energy converter: A validation of simulated buoy motions. Proc. Inst. Mech. Eng. Part M J. Eng. Marit. Environ. 232, 97–115. https://doi.org/10.1177/1475090217735954

Yu, L., Tan, J., 2005. Analysis of optimization for preliminary design of multi-component mooring systems. China Ocean Eng. 19, 299–308.

Zanganeh, R., Thiagarajan, K., 2018. Prediction of the mean heading of a turret moored FPSO in bi-modal and bi-directional sea states. Appl. Ocean Res. 78, 156–166. https://doi.org/10.1016/j.apor.2018.04.006

Zhao, W., Yang, J., Hu, Z., Wei, Y., 2013. Numerical investigation on the hydrodynamic difference between internal and external turret-moored FLNG. J. Shanghai Jiaotong Univ. 18, 590–597. https://doi.org/10.1007/s12204-011-1202-8

Zhao, Y., Dong, S., 2020. Design load estimation with IFORM-based models considering long-term extreme response for mooring systems. Ships Offshore Struct. https://doi.org/10.1080/17445302.2020.1838118